Monthly Notices of the ROYAL ASTRONOMICAL SOCIETY

MNRAS **531,** 2864–2880 (2024) https://doi.org/10.1093/mnras/stae1318
Advance Access publication 2024 May 23

INSPIRE: INvestigating Stellar Population In RElics – VI. The low-mass end slope of the stellar initial mass function and chemical composition

Michalina Maksymowicz-Maciata,[1]★ Chiara Spiniello ,[1,2]★ Ignacio Martín-Navarro,[3,4] Anna Ferré-Mateu ,[3,4] Davide Bevacqua ,[5,6] Michele Cappellari ,[1] Giuseppe D'Ago,[7,2] Crescenzo Tortora ,[2] Magda Arnaboldi,[8] Johanna Hartke ,[9,10] Nicola R. Napolitano,[11] Paolo Saracco [5] and Diana Scognamiglio[12]

[1]*Sub-Dep. of Astrophysics, Dep. of Physics, University of Oxford, Denys Wilkinson Building, Keble Road, Oxford OX1 3RH, United Kingdom*
[2]*INAF – Osservatorio Astronomico di Capodimonte, Via Moiariello 16, I-80131, Naples, Italy*
[3]*Instituto de Astrofísica de Canarias, Vía Láctea s/n, E-38205 La Laguna, Tenerife, Spain*
[4]*Departamento de Astrofisica, Universidad de La Laguna, E-38200, La Laguna, Tenerife, Spain*
[5]*INAF – Osservatorio Astronomico di Brera, Via Brera 28, I-20121 Milano, Italy*
[6]*DiSAT, Università degli Studi dell'Insubria, Via Valleggio 11, I-22100 Como, Italy*
[7]*Institute of Astronomy, University of Cambridge, Madingley Road, Cambridge CB3 0HA, United Kingdom*
[8]*European Southern Observatory, Karl-Schwarzschild-Straße 2, D-85748, Garching, Germany*
[9]*Finnish Centre for Astronomy with ESO (FINCA),, University of Turku, FI-20014, Turku, Finland*
[10]*Tuorla Observatory, Department of Physics and Astronomy, University of Turku, FI-20014, Turku, Finland*
[11]*Department of Physics 'Pancini' University of Naples Federico II C.U. di Monte Sant'Angelo Via Cintia ed. 6, I-80126 Naples, Italy*
[12]*Jet Propulsion Laboratory, California Institute of Technology, 4800, Oak Grove Drive - Pasadena, CA 91109, USA*

Accepted 2024 May 16. Received 2024 May 16; in original form 2024 January 28

ABSTRACT

The INSPIRE project has built the largest sample of ultra-compact massive galaxies (UCMGs) at $0.1 < z < 0.4$ and obtained their star formation histories (SFHs). Due to their preserved very old stellar populations, relics are the perfect systems to constrain the earliest epochs of mass assembly in the Universe and the formation of massive early-type galaxies. The goal of this work is to investigate whether a correlation exists between the degree of relicness (DoR), quantifying the fraction of stellar mass formed at $z > 2$, and the other stellar population parameters. We use the Full-Index-Fitting method to fit the INSPIRE spectra to single stellar population (SSP) models. This allows us to measure, for the first time, the slope of the IMF, as well as stellar metallicity [M/H], [Mg/Fe], [Ti/Fe], and [Na/Fe] ratios, and study correlations between them and the DoR. Similarly to normal-sized galaxies, UCMGs with larger stellar masses have overall higher metallicities. We found a correlation between the IMF slope and the DoR, that, however, breaks down for systems with a more extended SFH. An even stronger dependency is found between the IMF and the fraction of mass formed at high-z. At equal velocity dispersion and metallicity, galaxies with a higher DoR have a larger dwarf-to-giant ratio, i.e. a bottom heavy IMF, than that of low-DoR counterparts. This might indicate that the cosmic epoch and therefore different formation scenarios influence the fragmentation of the star formation cloud and hence might be the explanation for IMF variations detected in massive ETGs.

Key words: Galaxies: elliptical and lenticular, cD – Galaxies: evolution – Galaxies: formation – Galaxies: kinematics and dynamics – Galaxies: star formation – Galaxies: stellar content.

1 INTRODUCTION

More than half of the total stellar mass in the Universe is contained in massive early-type galaxies (ETGs; e.g. Renzini 2006, section 1), which play an essential role in the context of cosmic structure formation and evolution (Blumenthal et al. 1984). They host the oldest populations of stars, thus retaining the memory of the earliest star formation activity. However, in local, giant massive ETGs, this oldest population is contaminated by accreted and/or later formed stars.

Luckily, since galaxy interactions and mergers are stochastic phenomena, a small fraction of galaxies avoid the accretion and merging phase and retain their original stellar population and ultra-compact nature, becoming the *relics* of the ancient Universe (Trujillo et al. 2009). As relic galaxies can be observed at low redshifts with their structure intact, these 'sealed time-capsules' allow us to study the earliest cosmic epochs with the amount of detail only achievable in the nearby Universe. Studying relic galaxies can therefore help answer many questions about the early Universe and the formation and evolution of massive ETGs. This is the reason

★ E-mail: michalina.maksymowicz.maciata@gmail.com(MM); chiara.spiniello@physics.ox.ac.uk(CS)

why, in the last few years, ultra-compact massive galaxies (UCMGs) in general, and relics (very old UCMGs) more specifically, received a lot of attention from the scientific community (Trujillo et al. 2009; Taylor et al. 2010; Valentinuzzi et al. 2010; Shih & Stockton 2011; Trujillo, Carrasco & Ferré-Mateu 2012; Damjanov et al. 2013, 2014, 2015; Poggianti et al. 2013; Saulder, van den Bosch & Mieske 2015; Yıldırım et al. 2015, 2017; Tortora et al. 2016, 2018; Charbonnier et al. 2017; Buitrago et al. 2018; Martín-Navarro, van de Ven & Yıldırım 2019; Barbosa et al. 2021b; Flores-Freitas et al. 2022; Lisiecki et al. 2023; Lohmann et al. 2023; Siudek et al. 2023; Eappen & Kroupa 2024; Moura et al. 2024).

To date, only a dozen of relics have been confirmed and fully characterized at $z \sim 0$ (Trujillo et al. 2014; Yıldırım et al. 2015; Salvador-Rusiñol et al. 2021; Comerón et al. 2023).[1] From *Hubble Space Telescope* high-resolution imaging, the morphology and density profiles of local relics match those found in high-z passive UCMGs (Trujillo et al. 2014; Ferré-Mateu et al. 2017; Yıldırım et al. 2017). It has also been claimed that relics could be hosting über-massive black holes (Ferré-Mateu et al. 2015).

Only for three relics at $z \sim 0$ spatially resolved spectroscopy has been obtained (Ferré-Mateu et al. 2017). Kinematically, these three systems have large rotation velocities ($V \sim$ 200–300 km s^{-1}) and very high central stellar velocity dispersion values ($\sigma_\star >$ 300 km s^{-1}). Finally, from a stellar population point of view, they have very peaked and extremely high-z star formation histories (SFHs) and are populated by stars with supersolar metallicities ($Z \sim$ 0.2–0.3, with strong spatial gradients) and [Mg/Fe], old ages (∼13 Gyr), and a bottom-heavy (i.e. dwarf rich) initial mass function (IMF) slope (Martín-Navarro et al. 2015b; Ferré-Mateu et al. 2017).

To validate these results, a larger statistical sample is necessary, whilst enlarging the redshift boundaries outside the local Universe. This has been the goal of the INvestigating Stellar Populations In RElics (INSPIRE) Project. Targeting 52 spectroscopically confirmed UCMGs at $0.1 < z < 0.4$, all with effective radii $R_e < 2$ kpc and stellar masses $M_\star > 6 \times 10^{10}$ M$_\odot$, INSPIRE has built the largest sample of spectroscopically confirmed UCMGs with measured kinematics and stellar population parameters. Of these, 38 have been classified as relics, as they formed more than 75 per cent of their stellar masses already by $z > 2$. The survey has been presented in Spiniello et al. (2021a) and Spiniello et al. (2021b, hereafter INSPIRE DR1). In D'Ago et al. (2023, hereafter INSPIRE DR2), extensive tests were performed on the kinematics, deriving the stellar velocity dispersion within an aperture encapsulating 50 per cent of the light. However, since the spectra are fully seeing-dominated, and the seeing is much larger than the effective radii of the UCMGs, the velocity dispersion values have to be interpreted as lower limits.[2] Finally, the stellar populations analysis of the entire sample has been presented in Spiniello et al. (2023, hereafter INSPIRE DR3). In Ferré-Mateu et al. (2017) it was suggested that three local relics could be ranked from the most extreme to the least extreme, in terms of their morphological and stellar population characteristics, hence following a degree of relicness (DoR). Motivated by this finding, and thanks to the larger statistical sample, INSPIRE was able to quantify such DoR parameter, as a dimensionless number, varying from 0 to 1. The DoR is defined in terms of the fraction of stellar mass formed by $z = 2$ (assumed to be the end of the first phase; Zolotov et al. 2015), the cosmic time at which a galaxy has assembled 75 per cent of its mass and the final assembly time. According to this, galaxies with a high DoR are the most extreme relics as they assembled their stellar mass at the earliest epochs and very quickly, while low-DoR objects show a non-negligible fraction of later-formed populations and hence a spread in ages and metallicities. It was unambiguously found that at similar stellar masses, objects with a higher DoR have larger stellar metallicity and velocity dispersion values. However, the analysis in DR3 was done while keeping the elemental abundances fixed and assuming a universal IMF, which might not be the best assumption, given the results emerging in the last few years. Indeed, since the work by van Dokkum et al. (2010), increasing evidence has emerged supporting a non-universal IMF varying across galaxies (Treu et al. 2010; Cappellari et al. 2012, 2013b; Spiniello et al. 2012, 2014, 2015b; Conroy & van Dokkum 2012a; La Barbera et al. 2013; Tortora et al. 2013; Martín-Navarro et al. 2015c) and spatially within single massive objects (Martín-Navarro et al. 2015a; van Dokkum et al. 2017; Parikh et al. 2018; Sarzi et al. 2018; La Barbera et al. 2019; Barbosa et al. 2021b). The reason for these variations is however still debated.

For the three local relics, a bottom-heavy IMF (i.e. with a dwarf-to-giant stars ratio being at least a factor of 2 larger than that found in the Milky Way) has been inferred up to a few effective radii (Martín-Navarro et al. 2015b; Ferré-Mateu et al. 2017; Comerón et al. 2023). For normal-sized massive galaxies, instead, a similarly bottom-heavy IMF, with a fraction of stars with M $<$ 0.5 M$_\odot$ a factor of two larger than the one measured in the Milky Way, is only required in the innermost region (Martín-Navarro et al. 2015a; Parikh et al. 2018; Sarzi et al. 2018; La Barbera et al. 2019; Barbosa et al. 2021a). Here, according to the two-phase formation scenario, the relic component is supposed to dominate the light budget (Navarro-González et al. 2013; Pulsoni et al. 2021; Barbosa et al. 2021a). All these observations can be explained assuming that the IMF might have been bottom-heavy during the early stages of galaxy formation when the Universe was much more dense and richer in hot gas, but only if stars formed through a very intense (SFR $\geq 10^3$ M$_\odot$ yr^{-1}) and very short ($\tau \sim$ 100 Myr) burst (Chabrier, Hennebelle & Charlot 2014; Smith 2020; Barbosa et al. 2021a). Hence, in UCMGs with high DoR, where the great majority of the stellar mass was formed during the first phase at high-z, we should be able to measure a steep IMF slope even from an integrated spectrum covering a large portion of the galaxy size. Indeed this is what we preliminary found in Martín-Navarro et al. (2023), the fourth paper of the INSPIRE series (hereafter INSPIRE IV). Stacking the ultraviolet B (UVB) and visible (VIS) spectra of five relics and those of five non-relics with very similar velocity dispersion and metallicity values, we measured a systematic difference in the IMF slope which is dwarf-richer for relics. However, stacking spectra from different galaxies, broadened the final IMF probability density distribution (PDF), especially for non-relics, where the single stellar population (SSP) assumption could be less reliable, given the more heterogeneous and extended SFHs. Hence, a larger statistical sample is necessary to confirm this result. This is one of the main goals of this sixth paper of the INSPIRE series.

In this work, we carefully inspect one by one the 52 INSPIRE UCMGs, identifying contamination and bad pixels that could affect line-indices measurements. This allows us to derive the IMF slopes of each single object and study how they relate to their DoR and other stellar population and kinematical parameters. The paper is organized as follows. In Section 2, we introduce the data and explain the methods and analysis of the stellar populations. Section 3 presents the results and correlations between the obtained stellar population parameters. We then focus on the stellar velocity dispersion (Section 3.1), the metallicity (Section 3.2), and the IMF slope (Section 3.3) and

[1]The number depends on the mass and size threshold used to define relics.
[2]See appendix A in Spiniello et al. (2021b).

their correlations with the DoR, as well as with each other (Section 3.4). Finally, Section 4 is reserved for discussion, while in Section 5, we present our conclusions and summarize the findings of the paper.

Throughout this paper, we assume a standard Lambda cold dark matter (ΛCDM) cosmology with $H_0 = 69.6$ km s^{-1} Mpc^{-1}, $\Omega_\Lambda = 0.714$, and $\Omega_M = 0.286$ (Bennett et al. 2014).

2 DATA AND ANALYSIS

2.1 Observations

This work uses the sample of 52 UCMGs from the INSPIRE project, with data collected as part of an ESO Large Programme (LP, ID: 1104.B-0370, PI: C. Spiniello). The programme started in P104 (2019 October) and was completed in 2023 March, delivering high signal-to-noise ratio (SNR) spectra ($20 \leq$ SNR ≤ 80 per Å), from the UVB to the near-infrared (NIR), with the X-Shooter spectrograph (XSH; Vernet et al. 2011). We refer the readers to INSPIRE DR1 and INSPIRE DR3 for a comprehensive description of the sample selection and characteristics.

In this paper, we use the one-dimensional (1D) INSPIRE spectra extracted at the R50 radius. This radius is obtained considering the surface brightness profiles of the two-dimensional (2D) spectra (for each single observation block) and integrating them up to the aperture that encapsulates 50 per cent of the total light. However, because ground-based observations are seeing-limited, and the seeing is much larger than the galaxies' size, the aperture contains a mix of light from inside and outside the real effective radius. We refer the readers to INSPIRE DR1 for a more detailed description of the 1D extraction, which however plays an almost negligible role in the relic confirmation.

Moreover, we only consider the rest-framed and telluric-corrected combined UVB + VIS spectra smoothed at a final resolution of FWHM = 2.51 Å, matching that of the SSP models we use for the fitting (Sec.2.2). Our choice of not including the NIR is two-fold. First, the telluric contamination on the spectra in this wavelength range is much larger than the one affecting the VIS. Secondly, a detailed treatment of several individual element abundances, currently not included in the SSP models, is critical to properly fit the observed strengths of infrared absorption features, especially regarding Carbon-sensitive indices, which are systematically underestimated by the current SSP models (Eftekhari et al. 2022).

The characteristics of the INSPIRE, including coordinates, redshift, DoR, velocity dispersion values, and SNR inferred from the UVB and the VIS spectra, are reported in Table 1. The SNR of the spectra cover a wide range and it is generally higher in the optical, as expected for red galaxies with evolved stellar populations. In the last two columns of the table, we list the stellar masses and size of the 52 objects, taken from Tortora et al. (2018) and Scognamiglio et al. (2020).[3]

2.2 Stellar population models

We use the MILES SSP models developed and described in Vazdekis et al. (2015) with BaSTI (a Bag of Stellar Tracks and Isochrones) theoretical isochrones (Pietrinferni et al. 2004, 2006). The MILES SSPs are based on the MILES empirical stellar library[4] (Sánchez-Blázquez, Gorgas & Cardiel 2006; Falcón-Barroso et al. 2011), covering the wavelength range [3525–7500] Å. The SSPs cover a broad range of stellar ages, ranging from 30 Myr to 14 Gyr, and sampled at logarithmic steps, total stellar metallicities in the range $-2.27 <$ [M/H] $< +0.40$, two values of the [α/Fe] ratios (solar and supersolar, +0.4 dex), and a suite of stellar IMF slopes. For this paper, we use the bimodal IMF parametrization defined in Vazdekis et al. (1996). This is described by two power-law regimes with a break at 0.6 $M_\odot$, where the low-mass slope is fixed at 1.3 (Salpeter 1955), while the high-mass slope (Γ_b) is free to vary between 0.3 and 3.5 and therefore, by normalization, effectively changes the relative fraction of low-mass stars, with respect to giant stars. Having a steeper Γ_b effectively corresponds to a larger dwarf-to-giant ratio, which is the only quantity measurable from spectroscopic stellar population analysis in galaxies with old stars, where all stars with masses above few solar ones are long dead.

Since degeneracies exist between variation in the IMF slope and single elemental abundances (e.g. Spiniello et al. 2014), we need to fit for these as well. In particular, Sodium (Na) and Titanium (Ti) absorption features have been extensively used to measure the IMF in massive ETGs (Spiniello et al. 2012, 2014, 2015a; Conroy & van Dokkum 2012b; Ferreras et al. 2013; Parikh et al. 2018; Sarzi et al. 2018; La Barbera et al. 2019). To model the variation of Na and Ti, we use response functions of these two elements, computed using the SSP models of Conroy & van Dokkum (2012a, hereafter CvD). We follow similar prescriptions to these given in Spiniello, Trager & Koopmans (2015c). In particular, the response functions are computed by simply taking the ratio between two CvD spectra, with the same age, same IMF, and metallicity,[5] one with solar abundances and one with different [Na/Fe] or [Ti/Fe]. In this way, we are able to isolate the effect of changing the elemental abundance from the effect of changing other stellar population parameters. Specifically, in this case, we compute response functions for a 13.5 Gyr population, which is sufficiently similar to the expectations for our sample given the weak age dependence of elemental abundance corrections (e.g. Vazdekis et al. 2015). The conclusions presented here will not change if a slightly younger age (e.g. 10–11 Gyr) would have been used to obtain the response functions and this is enough to draw conclusions on the elemental abundances in relics.

2.3 Full-Index Fitting

The core of the modelling in this work revolves around the Full-Index Fitting method (FIF; Martín-Navarro et al. 2019, 2021), which is a hybrid approach between a more standard line strength analysis and full-spectrum fitting. Instead of calculating the equivalent widths of key absorption features or fitting every pixel across a wide wavelength range, this method fits every pixel within the index-band region of the selected key absorption features to the models, after normalizing the continuum using the index definition. This hybrid approach has lower SNR requirements than pure line strength, reduced computational time than full-spectrum fitting (Martín-Navarro et al. 2019), and allows to focus on well-tested and studied spectral regions, where the information about specific stellar population properties is concentrated.

[3]The R_e are the median value between the single-band ones inferred from *g*, *r*, and *i*. These are obtained by fitting a point spread function (PSF) convolved Sérsic profile to the images using the code 2DPHOT (La Barbera et al. 2008).

[4]Publicly available at http://miles.iac.es.

[5]Note that the corrections are computed only for a Milky Way like IMF and at solar metallicity. We stress that the effects are degenerate. For instance, La Barbera et al. (2017) have shown that the response of the Na-dependent spectral indices to [Na/Fe] is stronger when the IMF is bottom-heavier.

Table 1. The INSPIRE sample. From left to right we give the coordinates, redshift, DoR, stellar velocity dispersion, SNR (per Å) in the UVB and VIS arms, the stellar mass inferred from SED fitting in the *ugri* bands, and the median effective radius in kpc (computed from the measurements in *g*, *r*, and *i* bands). These two last quantities are taken from Tortora et al. (2018) and Scognamiglio et al. (2020), while all the others are taken from INSPIRE DR3. Finally, in the last column, we report whether the galaxy is in the *Golden Sample*, as defined in Section 2.3.

ID	RA J2000	Dec. J2000	z	DoR	$\sigma_\star$ (km s^{-1})	SNR UVB	SNR VIS	$\langle R_e \rangle$ (kpc)	$M_\star$ ($10^{11} M_\odot$)	*Golden Sample*
J0211−3155	32.8962202	−31.9279437	0.3012	0.72	245 ± 25	13.9	46.7	1.07	0.88	Yes
J0224−3143	36.0902655	−31.7244923	0.3839	0.56	283 ± 14	20.9	71.2	1.55	2.71	Yes
J0226−3158	36.5109217	−31.9810149	0.2355	0.12	185 ± 19	22.9	58.7	1.32	0.69	Yes
J0240−3141	40.0080971	−31.6950406	0.2789	0.43	216 ± 22	17.9	54.5	0.81	0.98	No
J0314−3215	48.5942558	−32.2632678	0.2874	0.42	178 ± 9	20.7	54.6	0.66	1.00	Yes
J0316−2953	49.1896388	−29.8835868	0.3596	0.40	192 ± 19	14.3	46.4	1.02	0.87	Yes
J0317−2957	49.4141028	−29.9561748	0.2611	0.51	187 ± 19	20.1	51.7	1.05	0.87	No
J0321−3213	50.2954390	−32.2221290	0.2947	0.37	211 ± 11	21.9	66.4	1.37	1.23	Yes
J0326−3303	51.5140585	−33.0540443	0.297	0.25	173 ± 17	21.4	54.5	1.43	0.93	Yes
J0838+0052	129.5304520	0.8823841	0.2702	0.54	189 ± 9	22.6	65.2	1.28	0.87	Yes
J0842+0059	130.6665506	0.9899186	0.2959	0.73	324 ± 32	12.4	41.5	1.01	0.91	No
J0844+0148	131.0553886	1.8132204	0.2837	0.45	224 ± 22	12.9	45.0	1.14	0.71	Yes
J0847+0112	131.9112386	1.2057129	0.1764	0.83	244 ± 12	24.6	77.5	1.37	0.99	Yes
J0857−0108	134.2512185	−1.1457077	0.2694	0.39	166 ± 17	15.7	43.3	1.40	1.00	Yes
J0904−0018	136.0518949	−0.3054848	0.2989	0.32	205 ± 21	12.6	44.3	1.16	1.30	No
J0909+0147	137.3989150	1.7880025	0.2151	0.79	401 ± 20	20.7	75.3	1.05	1.05	Yes
J0917−0123	139.2701850	−1.3887918	0.3602	0.44	239 ± 24	12.2	50.3	1.37	2.19	Yes
J0918+0122	139.6446428	1.3794780	0.3731	0.43	242 ± 12	17.6	70.2	1.71	2.26	Yes
J0920+0126	140.1291393	1.4431610	0.3117	0.25	190 ± 19	17.9	55.6	1.51	0.98	Yes
J0920+0212	140.2320835	2.2126831	0.28	0.64	246 ± 25	17.0	55.0	1.48	1.03	No
J1026+0033	156.7231818	0.5580980	0.1743	0.29	225 ± 11	38.9	113.6	1.02	1.48	Yes
J1040+0056	160.2152308	0.9407580	0.2716	0.77	240 ± 24	11.5	46.7	1.29	0.93	Yes
J1114+0039	168.6994335	0.6510299	0.3004	0.40	181 ± 18	19.5	54.0	1.52	1.62	No
J1128−0153	172.0885023	−1.8890642	0.2217	0.34	192 ± 10	21.1	69.2	1.27	1.30	Yes
J1142+0012*	175.7023296	0.2043419	0.1077	0.18	129 ± 6	57.9	124.1	1.40	0.84	No
J1154−0016	178.6922829	−0.2779248	0.3356	0.11	163 ± 16	16.6	42.8	1.06	0.64	Yes
J1156−0023	179.2186145	−0.3946596	0.2552	0.30	177 ± 18	22.6	60.9	1.04	1.39	No
J1202+0251	180.5132277	2.8515451	0.3298	0.36	165 ± 17	14.7	45.9	1.49	0.68	Yes
J1218+0232	184.7355807	2.5449139	0.308	0.45	171 ± 17	14.6	42.0	1.40	0.93	Yes
J1228−0153	187.0640987	−1.8989049	0.2973	0.39	191 ± 10	23.2	70.1	1.61	1.15	Yes
J1402+0117	210.7400749	1.2917747	0.2538	0.31	166 ± 25	12.4	34.0	0.68	0.66	Yes
J1411+0233	212.8336012	2.5618381	0.3598	0.41	217 ± 11	24.1	73.2	1.07	1.55	Yes
J1412−0020	213.0038281	−0.3440699	0.2783	0.61	339 ± 51	10.5	31.1	1.42	1.20	No
J1414+0004	213.5646898	0.0809744	0.303	0.36	205 ± 31	11.7	37.4	1.42	1.18	Yes
J1417+0106	214.3685124	1.1073909	0.1794	0.33	203 ± 10	39.9	107.7	1.48	0.91	Yes
J1420-0035	215.1715599	−0.5864629	0.2482	0.41	209 ± 31	13.4	39.8	1.35	0.99	Yes
J1436+0007	219.0481314	0.1217459	0.221	0.33	193 ± 19	21.1	67.2	1.40	1.15	Yes
J1438−0127	219.5218882	−1.4582727	0.2861	0.78	218 ± 22	17.9	59.4	1.20	0.88	Yes
J1447−0149	221.9657402	−1.8242806	0.2074	0.38	187 ± 9	24.7	64.7	1.51	0.86	No
J1449−0138	222.3504660	−1.6459975	0.2655	0.60	192 ± 29	10.2	40.3	1.44	1.03	Yes
J1456+0020	224.2361596	0.3353906	0.2738	0.17	194 ± 29	11.9	39.6	0.50	0.71	No
J1457−0140	224.3397592	−1.6691725	0.3371	0.47	203 ± 30	12.5	34.1	1.66	1.51	Yes
J1527−0012	231.7772381	−0.2065670	0.4	0.38	237 ± 36	7.1	32.7	1.26	1.74	Yes
J1527−0023	231.7522351	−0.3997483	0.3499	0.37	188 ± 28	9.0	30.4	1.12	1.15	Yes
J2202−3101	330.5472803	−31.018381	0.3185	0.48	221 ± 22	13.1	47.6	1.45	1.10	Yes
J2204−3112	331.2228147	−31.200261	0.2581	0.78	227 ± 23	14.4	54.1	1.39	0.90	Yes
J2257−3306	344.3966471	−33.114445	0.2575	0.27	185 ± 19	17.8	40.0	1.18	0.93	No
J2305−3436	346.3356634	−34.603091	0.2978	0.80	295 ± 30	14.3	46.8	1.29	0.86	No
J2312−3438	348.2389042	−34.648591	0.3665	0.36	221 ± 11	32.1	72.4	1.25	1.34	Yes
J2327−3312	351.9910156	−33.200760	0.4065	0.06	227 ± 11	19.6	72.8	1.51	1.57	Yes
J2356−3332	359.1261248	−33.533475	0.3389	0.44	162 ± 24	11.5	34.2	1.06	0.98	Yes
J2359−3320	359.9851685	−33.333583	0.2888	0.71	267 ± 27	15.6	49.1	1.04	1.07	Yes

We use FIF in combination with the Penalized Pixel-fitting software[6] (PPXF; Cappellari & Emsellem 2004; Cappellari 2017, 2023), already used in previous INSPIRE publications. Specifically, we first run PPXF on the UVB + VIS combined and smoothed spectra, computing the stellar velocity dispersion, as well as the light-weighted stellar age (in logarithmic scale) and metallicity, and a first guess of the IMF slope. We note that we have customized the publicly available version of the code to let it constrain also the slope of the IMF, but we keep elemental abundance ratios fixed to solar and

[6] https://pypi.org/project/ppxf/

we do not fit for them. Moreover, we stress that in INSPIRE DR3 we performed two separate runs, one for kinematics and one for stellar population constraints. Here instead, we perform a single run. We, therefore believe that, although we obtain the stellar velocity dispersion as a bi-product, the values computed in DR3 are more trustable, as the PPXF code was optimized for kinematics (e.g. using an additive polynomial and performing tests on the systematics and random errors). Hence, we list the DR3 values in Table 1 and plot and use these values throughout this paper. We nevertheless show in Appendix B that the agreement between the two measurements is good (see the right-most panel of Fig. B1).

Following the same line of thoughts, we did not rederive the DoR here based on the new ages and metallicities computed with PPXF. Indeed, we did not perform any regularization during the fit (see INSPIRE DR3 for details), which often revealed signs of younger ages, when there, as in the case of systems with low DoR. We, therefore, believe that the DoR computed in INSPIRE DR3 is more correct and use that for the remainder of this paper.

At this point, we input the best-fitting age and the velocity dispersion values to the FIF routine as fixed values and obtain an estimate for the stellar metallicity, Mg, Na, and Ti abundances, and the IMF slope (Γ_b) with their associated uncertainties. We use the [α/Fe] from the MILES models as a proxy for [Mg/Fe]. This is motivated by the fact that even though the models are built at varying [α/Fe] the α element we are most sensitive to in the wavelength range we use, is Magnesium. Indeed, although TiO bands also depend on [α/Fe], this effect is counter-balanced by the sensitivity to Carbon and by the fact that we also allow for [Ti/Fe] variation. Therefore, hereafter, we will always quote and refer to [Mg/Fe] ratios.

Note that, although the model grid is in principle discrete, the best-fitting stellar population values and uncertainties are estimated by linearly interpolating the closest nodes in the grid.

Following Martín-Navarro et al. (2019), the age is kept fixed for this second step to the one obtained with PPXF, in order to circumvent the effect of [C/Fe] on the strength of the H β feature (Conroy & van Dokkum 2012a). In practice, this approach minimizes any potential [C/Fe]-age degeneracy (Martín-Navarro et al. 2019) but this also means that we are ignoring any covariance between fitted IMF and age (or between abundance and age), leading to a possible underestimation of the final errors. We therefore have performed a FIF run letting the age free to vary and including one or more age-sensitive lines (e.g. Balmer lines) and another run where we fix the age to that obtained in DR3. More details on these tests are given in Appendix A, where we find that fitting also for age has a significant impact on the metallicity and Titanium abundance, especially at low and intermediate DoR, while the slope of the IMF and other chemical abundances changed only by a small amounts.

In principle, the larger the number of indices fitted, the better the constraining power should be (Spiniello et al. 2014). However, some of the optical spectral indices for several galaxies in the INSPIRE sample are contaminated by residuals of skylines and bad pixels, rendering them unfit to use. Hence, we need to select the minimum number of indices that allow us to break the degeneracy between the stellar population parameters while maximizing the number of galaxies without any signs of contamination. After extensive testing (see Appendix A), we selected six optical indices, namely Mgb, Fe5270, Fe5335, NaD, TiO1, and TiO2,[7] defined around stellar absorption features mainly coming from four different chemical species: Magnesium, Iron, Titanium, and Sodium. These are shown in the top panels of Fig. 1. In the corresponding bottom panels, we showcase how they respond to changes to the studied stellar population parameters. The combination of these six indices allows us to break the degeneracies among the stellar population parameters and enables us to correctly measure stellar metallicity, IMF slope, Mg, Na, and Ti abundances.

Starting from these six indices, and checking galaxy by galaxy whether the spectra present bad pixels and contaminated regions affecting the calculation of the equivalent width, we define a *Golden Sample* of 39 galaxies, for which none of the six selected features is contaminated (see last column of Table 1).

In Appendix A, we present a series of tests aimed at checking whether the results of the FIF depend on the spectral indices chosen to be fitted to the models, and which parameters are let free in the run. The main conclusion of these tests is that the only two significant differences in the inferred stellar population parameters arise when (i) changing the Mg index used for the fit (from Mgb to Mg2), or (ii) letting the age free to vary, adding a Balmer line to constrain it. However, importantly, the inference on the IMF is run-independent and therefore very robust and the results are almost completely unchanged for extreme relics, while a larger variation is found for galaxies with lower DoR.

2.4 Testing the SSP assumption

We remind the readers that PPXF uses a SERIES of SSPs to derive the SFH of a galaxy. For extreme relics, when the entire totality of the stellar mass has been formed quickly at very early cosmic time, it is expected that the code only uses a low number of very old SSPs. At decreasing DoR, the fraction of mass formed during the first phase of the formation scenario becomes smaller and the SFH more extended. Hence the number of SSP models, with different ages and metallicities, used for the fit increases. This also means that the assumption that the SFH can be reconstructed by combining SSP is less solid. In this section, we investigate the spread in age that PPXF attributes to each galaxy and how this correlates with the DoR obtained in INSPIRE DR3. We believe that the age spread represents a qualitative way to measure the validity of the SSP assumption: the larger the number of age-bins is, the worse an SSP approximation is for a given galaxy.

Fig. 2 presents how the DoR correlates with the maximum sum of the weights of five neighbouring bins of the age-distribution histogram (sum_5). To compute this number, we start by taking all the non-zero weights that PPXF has attributed to the array of SSP models (with different ages and metallicities). Then, marginalizing over metallicity, we produce an age-distribution histogram. From it, we calculate the sum of weights attributed by PPXF to every five neighbouring age-bins (corresponding to 2.5 Gyr, given that the models span an age grid of 0.5 Gyr), and check which group of five holds the greatest sum of their weights. As expected a clear correlation is found. Moreover, we also note that sum_5 effectively saturates for galaxies with DoR > 0.5. In the right panel of the same figure, we sketch the age distribution for different age bins. The threshold of 0.95, indicated with the horizontal dashed lines, corresponds to a very peaked distribution of ages above 9 Gyr, without any second peak at lower redshift (younger ages). Below $\mathrm{sum}_5 \sim 0.95$, the age histograms start to be broader, and then for $\mathrm{sum}_5 \leq 0.7$ peaks at younger ages appear and therefore the SSP-assumption becomes less valid. This value nicely corresponds to a DoR ~ 0.34, which was set as limit in INSPIRE DR3 to separate relics from non-relics.

[7]The indices definition, including also blue and red bandpasses are given in Table C1, in Appendix C.

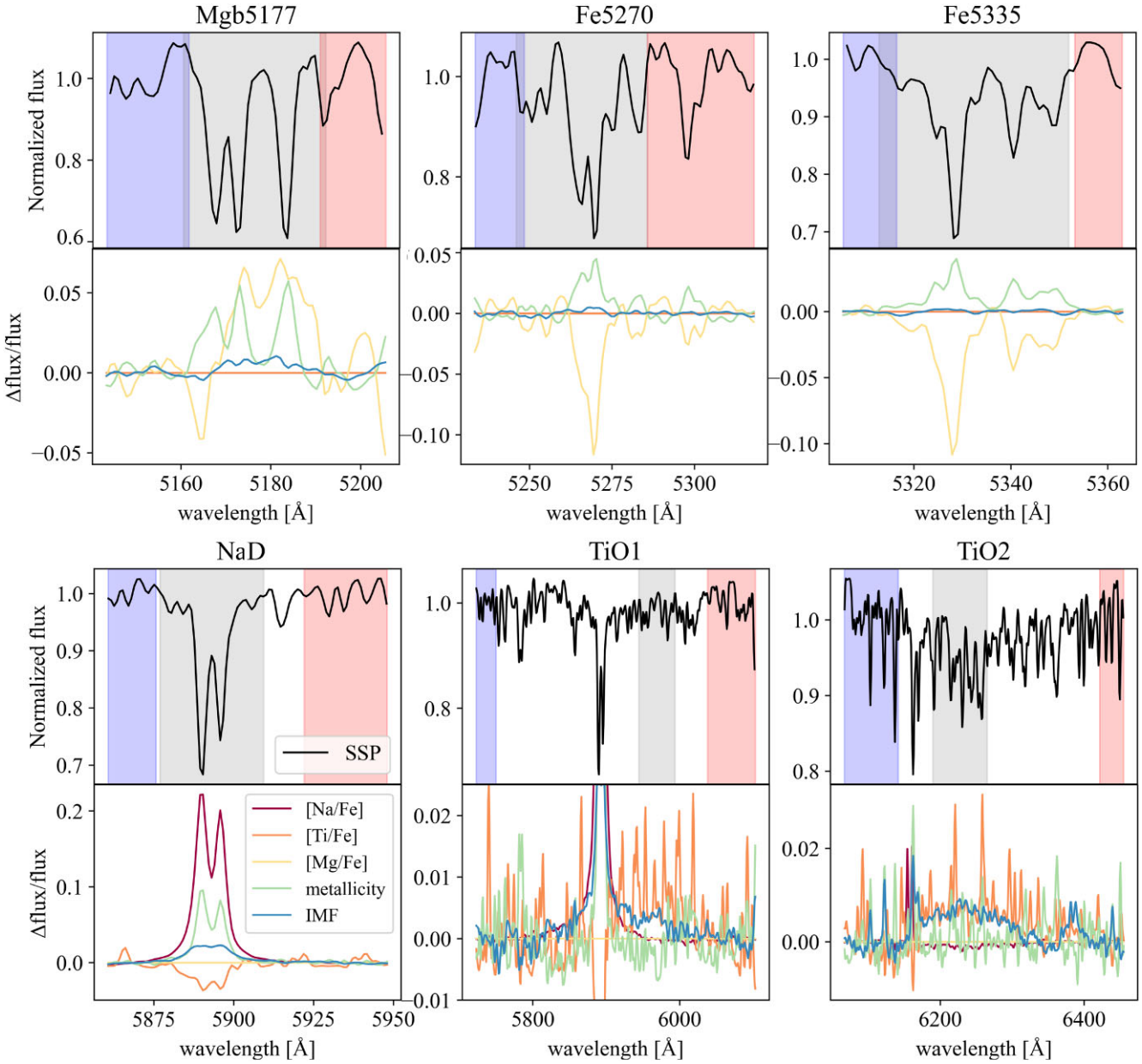

Figure 1. The six indices constituting our fiducial set: Mgb, Fe5270, and Fe5335 (top line) and NaD, TiO1, and TiO2 (bottom line). For each index, the top panel shows the index (grey, central shaded region) and blue and red bands (side shaded regions) around which the flux is normalized. The black lines correspond to model spectra of solar metallicity [M/H] = 0, [Mg/Fe] = 0, [Ti/Fe] = −0.3, [Na/Fe] = −0.3, and IMF slope of $\Gamma_B = 1.3$. The bottom panels show the relative change in the spectrum after varying different stellar population parameters: the IMF slope was varied by $\Delta\Gamma_B = 1$, the metallicity by 0.4 dex, and the different abundance ratios by 0.6 dex each.

We note that even though the sum_5 strongly correlated with the DoR for similar, intermediate DoR (0.4–0.6), different galaxies can have different sum_5. In the remainder of this paper, we will use the threshold of $\text{sum}_5 > 0.95$ to derive relations between stellar population parameters that might hold only for stars formed through a quick star formation episode at early cosmic time. We note that the threshold choice is arbitrary and different relations could be found based on different definitions, however, we believe it to be informative to check whether the correlations hold especially for the most strict age-distribution constraints. Furthermore, we acknowledge that the sum of the weights expresses a concept which is very similar to that measured with the DoR, but we note that the fitting assumptions within PPXF are different between this paper and the INSPIRE DR3 (see Appendix B for more details). Hence, the strong correlation between sum_5 computed here and the DoR computed in DR3 gives a nice evidence of the robustness of the stellar population results.

3 STELLAR POPULATION ANALYSIS RESULTS

This section presents the main results of the FIF analysis in terms of stellar population parameters and their relation with the DoR, obtained in INSPIRE DR3. A direct comparison with the results obtained in DR3 is presented in Appendix B. When not otherwise

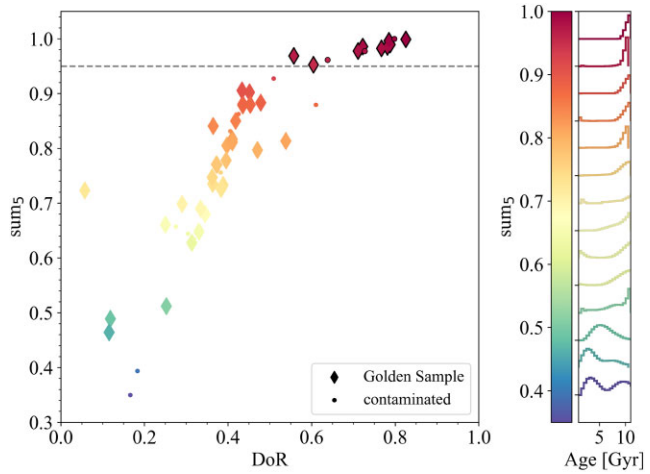

Figure 2. The DoR against the maximum sum of the weights held by five neighbouring bins in the age distribution histograms. Dashed line marks the 0.95 threshold of the sum of weights. On the right-most panel a sample of age-distributions is presented for a quick reference.

specified, we will focus on results obtained from the fiducial run, which are listed in Table 2.

Fig. 3 summarizes the results of the FIF analysis and also shows how the stellar population parameters correlate with stellar mass, size, and velocity dispersion of the INSPIRE objects. The objects are colour-coded by DoR but the only two parameters that seem to correlate with the DoR are metallicity (no red points at sub-solar values) and velocity dispersion (no red points at lower values), as already hinted for in INSPIRE DR3 and further shown in Section 3.1. More specifically, relics, and especially extreme relics have systematically larger stellar velocity dispersion than non-relics. For the metallicity, there is a large scatter but, all the extreme relics have supersolar [M/H] and a hint for a correlation can be seen. This will be further investigated in Section 3.2. No colour-clustering is found instead for the considered elemental abundances (Mg, Na, and Ti).[8] We caution the readers that the physical interpretation for single elemental abundance might not be straightforward, both because of the SNR of the data and the uncertainties in the models. This is especially true for the TiO molecular bands, since the line lists feeding the response functions from the CvD models are incomplete, and these broad features also depend on other elements, such as Carbon. Nevertheless, we need to fit for them in order to break the IMF-elemental abundance degeneracy (e.g. Spiniello et al. 2015c).

Another interesting result is that while a scatter exists in the sizes and masses of the entire sample, although they are selected to be similarly ultra-compact and massive, the most extreme relics cluster around $R_e \sim 1$ kpc and ~ 1–1.5×10^{11} $M_\odot$. Nevertheless, we stress that only with higher spatial resolution data (e.g. from space or using adaptive-optics-supported ground telescopes) we can obtain a more precise and robust estimate of the size of these objects.

[8]We note that in DR1 and DR3 we found a correlation between the DoR and the [Mg/Fe], estimated via line-indices. However, as already reported in Barbosa et al. (2021b), the estimates obtained via different techniques do not match.

Table 2. Stellar population results from FIF for the fiducial model.

ID	Γ_b	[M/H]	[Mg/Fe]	[Ti/Fe]	[Na/Fe]
J0211−3155	$1.71^{+0.30}_{-0.32}$	$-0.06^{+0.06}_{-0.06}$	$0.07^{+0.06}_{-0.04}$	$-0.23^{+0.09}_{-0.06}$	$0.06^{+0.07}_{-0.08}$
J0224−3143	$0.88^{+0.32}_{-0.35}$	$0.14^{+0.04}_{-0.03}$	$0.22^{+0.05}_{-0.04}$	$-0.26^{+0.04}_{-0.02}$	$0.28^{+0.01}_{-0.03}$
J0226−3158	$1.54^{+0.39}_{-0.44}$	$-0.47^{+0.05}_{-0.05}$	$0.17^{+0.07}_{-0.07}$	$-0.24^{+0.15}_{-0.09}$	$0.18^{+0.05}_{-0.05}$
J0240−3141	$1.75^{+0.44}_{-0.41}$	$0.36^{+0.03}_{-0.04}$	$0.08^{+0.04}_{-0.04}$	$-0.28^{+0.04}_{-0.02}$	$0.05^{+0.08}_{-0.10}$
J0314−3215	$1.14^{+0.41}_{-0.39}$	$0.01^{+0.07}_{-0.05}$	$0.01^{+0.02}_{-0.01}$	$-0.20^{+0.13}_{-0.09}$	$0.24^{+0.04}_{-0.05}$
J0316−2953	$1.76^{+0.38}_{-0.44}$	$-0.33^{+0.10}_{-0.07}$	$0.07^{+0.06}_{-0.05}$	$-0.24^{+0.08}_{-0.04}$	$0.27^{+0.02}_{-0.04}$
J0317−2957	$2.55^{+0.35}_{-0.71}$	$0.06^{+0.04}_{-0.03}$	$0.23^{+0.07}_{-0.06}$	$0.27^{+0.03}_{-0.05}$	$0.12^{+0.09}_{-0.08}$
J0321−3213	$1.24^{+0.30}_{-0.30}$	$0.11^{+0.06}_{-0.05}$	$0.07^{+0.04}_{-0.04}$	$-0.26^{+0.06}_{-0.02}$	$0.00^{+0.07}_{-0.07}$
J0326−3303	$1.80^{+0.29}_{-0.36}$	$-0.11^{+0.05}_{-0.05}$	$0.12^{+0.06}_{-0.06}$	$-0.19^{+0.14}_{-0.09}$	$-0.04^{+0.06}_{-0.06}$
J0838+0052	$2.20^{+0.29}_{-0.40}$	$0.07^{+0.03}_{-0.02}$	$0.15^{+0.04}_{-0.04}$	$0.28^{+0.02}_{-0.04}$	$-0.03^{+0.05}_{-0.06}$
J0842+0059	$2.80^{+0.26}_{-0.32}$	$0.36^{+0.03}_{-0.04}$	$0.26^{+0.06}_{-0.06}$	$-0.18^{+0.16}_{-0.10}$	$0.27^{+0.02}_{-0.05}$
J0844+0148	$2.70^{+0.25}_{-0.26}$	$-0.19^{+0.05}_{-0.05}$	$0.16^{+0.06}_{-0.06}$	$0.01^{+0.16}_{-0.18}$	$0.24^{+0.04}_{-0.06}$
J0847+0112	$2.44^{+0.25}_{-0.37}$	$0.09^{+0.06}_{-0.06}$	$0.20^{+0.05}_{-0.05}$	$0.12^{+0.20}_{-0.16}$	$0.26^{+0.03}_{-0.05}$
J0857−0108	$0.79^{+0.41}_{-0.32}$	$-0.02^{+0.05}_{-0.05}$	$0.36^{+0.03}_{-0.05}$	$0.18^{+0.10}_{-0.16}$	$-0.20^{+0.06}_{-0.05}$
J0904−0018	$1.79^{+0.37}_{-0.42}$	$0.00^{+0.06}_{-0.06}$	$0.13^{+0.07}_{-0.06}$	$-0.20^{+0.13}_{-0.07}$	$0.04^{+0.07}_{-0.08}$
J0909+0147	$2.35^{+0.23}_{-0.28}$	$0.20^{+0.05}_{-0.05}$	$0.12^{+0.05}_{-0.05}$	$-0.04^{+0.17}_{-0.11}$	$0.27^{+0.02}_{-0.04}$
J0917−0123	$2.52^{+0.44}_{-0.68}$	$0.21^{+0.06}_{-0.07}$	$0.23^{+0.06}_{-0.06}$	$-0.24^{+0.16}_{-0.07}$	$0.29^{+0.01}_{-0.01}$
J0918+0122	$1.61^{+0.33}_{-0.36}$	$-0.06^{+0.05}_{-0.04}$	$0.26^{+0.05}_{-0.05}$	$-0.24^{+0.08}_{-0.04}$	$0.21^{+0.05}_{-0.04}$
J0920+0126	$0.67^{+0.27}_{-0.25}$	$-0.15^{+0.04}_{-0.04}$	$0.12^{+0.05}_{-0.05}$	$-0.25^{+0.07}_{-0.03}$	$0.10^{+0.04}_{-0.05}$
J0920+0212	$2.30^{+0.37}_{-0.44}$	$0.25^{+0.06}_{-0.06}$	$0.14^{+0.05}_{-0.05}$	$-0.22^{+0.12}_{-0.06}$	$0.02^{+0.10}_{-0.11}$
J1026+0033	$2.63^{+0.13}_{-0.15}$	$0.20^{+0.02}_{-0.02}$	$0.21^{+0.03}_{-0.03}$	$-0.29^{+0.01}_{-0.01}$	$0.30^{+0.00}_{-0.00}$
J1040+0056	$3.02^{+0.18}_{-0.23}$	$0.12^{+0.05}_{-0.05}$	$0.25^{+0.05}_{-0.05}$	$0.22^{+0.08}_{-0.13}$	$-0.16^{+0.09}_{-0.08}$
J1114+0039	$1.32^{+0.46}_{-0.42}$	$-0.45^{+0.05}_{-0.05}$	$0.39^{+0.00}_{-0.01}$	$-0.21^{+0.14}_{-0.09}$	$0.26^{+0.03}_{-0.04}$
J1128−0153	$0.73^{+0.26}_{-0.25}$	$0.08^{+0.03}_{-0.04}$	$0.04^{+0.03}_{-0.03}$	$-0.25^{+0.06}_{-0.03}$	$0.29^{+0.01}_{-0.02}$
J1142+0012	$3.28^{+0.01}_{-0.04}$	$-0.46^{+0.03}_{-0.03}$	$0.03^{+0.04}_{-0.02}$	$-0.30^{+0.01}_{-0.00}$	$0.30^{+0.00}_{-0.00}$
J1154−0016	$1.39^{+0.50}_{-0.49}$	$0.25^{+0.07}_{-0.07}$	$0.05^{+0.05}_{-0.03}$	$0.00^{+0.06}_{-0.11}$	$0.14^{+0.06}_{-0.07}$
J1156−0023	$1.45^{+0.29}_{-0.26}$	$0.11^{+0.04}_{-0.03}$	$0.01^{+0.02}_{-0.01}$	$-0.29^{+0.03}_{-0.01}$	$-0.03^{+0.05}_{-0.05}$
J1202+0251	$0.94^{+0.35}_{-0.32}$	$-0.07^{+0.05}_{-0.05}$	$0.05^{+0.05}_{-0.04}$	$-0.23^{+0.10}_{-0.05}$	$0.03^{+0.06}_{-0.05}$
J1218+0232	$1.57^{+0.47}_{-0.48}$	$-0.13^{+0.05}_{-0.05}$	$0.12^{+0.06}_{-0.06}$	$0.03^{+0.17}_{-0.18}$	$0.14^{+0.07}_{-0.08}$
J1228−0153	$0.79^{+0.37}_{-0.32}$	$0.03^{+0.04}_{-0.04}$	$0.17^{+0.04}_{-0.04}$	$-0.19^{+0.12}_{-0.09}$	$0.06^{+0.05}_{-0.05}$
J1402+0117	$0.83^{+0.44}_{-0.34}$	$-0.47^{+0.07}_{-0.07}$	$0.11^{+0.10}_{-0.08}$	$-0.20^{+0.17}_{-0.10}$	$0.20^{+0.06}_{-0.08}$
J1411+0233	$1.97^{+0.33}_{-0.28}$	$-0.19^{+0.04}_{-0.11}$	$0.13^{+0.05}_{-0.05}$	$-0.21^{+0.10}_{-0.05}$	$0.28^{+0.01}_{-0.02}$
J1412−0020	$1.54^{+0.36}_{-0.39}$	$-0.08^{+0.10}_{-0.07}$	$0.02^{+0.03}_{-0.01}$	$-0.19^{+0.08}_{-0.05}$	$0.28^{+0.01}_{-0.04}$
J1414+0004	$0.99^{+0.44}_{-0.38}$	$-0.12^{+0.06}_{-0.06}$	$0.27^{+0.06}_{-0.06}$	$-0.24^{+0.06}_{-0.03}$	$0.28^{+0.01}_{-0.02}$
J1417+0106	$0.62^{+0.27}_{-0.22}$	$-0.12^{+0.02}_{-0.02}$	$0.11^{+0.03}_{-0.03}$	$0.16^{+0.07}_{-0.10}$	$0.08^{+0.03}_{-0.03}$
J1420−0035	$1.30^{+0.43}_{-0.46}$	$-0.32^{+0.07}_{-0.06}$	$0.21^{+0.09}_{-0.08}$	$-0.18^{+0.17}_{-0.10}$	$0.25^{+0.03}_{-0.05}$
J1436+0007	$2.65^{+0.28}_{-0.29}$	$-0.12^{+0.04}_{-0.04}$	$0.05^{+0.04}_{-0.04}$	$0.08^{+0.13}_{-0.22}$	$-0.04^{+0.08}_{-0.09}$
J1438−0127	$2.47^{+0.24}_{-0.31}$	$0.17^{+0.04}_{-0.05}$	$0.18^{+0.04}_{-0.04}$	$0.19^{+0.07}_{-0.15}$	$-0.16^{+0.08}_{-0.08}$
J1447−0149	$2.25^{+0.50}_{-0.77}$	$0.32^{+0.04}_{-0.04}$	$0.01^{+0.01}_{-0.01}$	$0.25^{+0.04}_{-0.07}$	$-0.13^{+0.09}_{-0.09}$
J1449−0138	$2.15^{+0.40}_{-0.49}$	$-0.20^{+0.05}_{-0.05}$	$0.22^{+0.06}_{-0.06}$	$0.21^{+0.06}_{-0.12}$	$0.07^{+0.07}_{-0.08}$
J1456+0020	$1.53^{+0.85}_{-0.84}$	$-0.07^{+0.06}_{-0.05}$	$0.01^{+0.02}_{-0.01}$	$0.27^{+0.03}_{-0.05}$	$0.19^{+0.06}_{-0.07}$
J1457−0140	$0.80^{+0.32}_{-0.30}$	$-0.13^{+0.07}_{-0.07}$	$0.04^{+0.05}_{-0.03}$	$-0.16^{+0.20}_{-0.14}$	$0.15^{+0.08}_{-0.08}$
J1527−0012	$1.05^{+0.48}_{-0.40}$	$-0.10^{+0.07}_{-0.07}$	$0.13^{+0.10}_{-0.08}$	$0.11^{+0.19}_{-0.21}$	$0.26^{+0.03}_{-0.05}$
J1527−0023	$3.21^{+0.06}_{-0.12}$	$-0.19^{+0.08}_{-0.07}$	$0.10^{+0.09}_{-0.07}$	$-0.24^{+0.11}_{-0.06}$	$0.28^{+0.01}_{-0.03}$
J2202−3101	$0.67^{+0.39}_{-0.25}$	$0.26^{+0.05}_{-0.05}$	$0.13^{+0.04}_{-0.04}$	$0.03^{+0.16}_{-0.17}$	$-0.05^{+0.08}_{-0.09}$
J2204−3112	$3.12^{+0.12}_{-0.14}$	$0.07^{+0.05}_{-0.05}$	$0.08^{+0.05}_{-0.05}$	$0.26^{+0.05}_{-0.10}$	$0.24^{+0.04}_{-0.07}$
J2257−3306	$2.59^{+0.35}_{-0.40}$	$-0.16^{+0.06}_{-0.06}$	$0.37^{+0.02}_{-0.04}$	$0.21^{+0.08}_{-0.16}$	$-0.03^{+0.09}_{-0.09}$
J2305−3436	$2.28^{+0.32}_{-0.35}$	$0.32^{+0.05}_{-0.06}$	$0.10^{+0.06}_{-0.05}$	$-0.23^{+0.10}_{-0.05}$	$0.25^{+0.04}_{-0.07}$
J2312−3438	$1.30^{+0.35}_{-0.34}$	$-0.10^{+0.04}_{-0.04}$	$0.11^{+0.05}_{-0.05}$	$-0.10^{+0.14}_{-0.08}$	$0.20^{+0.05}_{-0.05}$
J2327−3312	$0.88^{+0.41}_{-0.34}$	$0.05^{+0.05}_{-0.06}$	$0.04^{+0.04}_{-0.03}$	$-0.18^{+0.18}_{-0.12}$	$0.18^{+0.06}_{-0.05}$
J2356−3332	$1.24^{+0.53}_{-0.48}$	$0.09^{+0.08}_{-0.08}$	$0.32^{+0.05}_{-0.07}$	$0.09^{+0.13}_{-0.19}$	$0.13^{+0.09}_{-0.10}$
J2359−3320	$2.55^{+0.27}_{-0.30}$	$-0.07^{+0.06}_{-0.06}$	$0.32^{+0.05}_{-0.07}$	$0.14^{+0.16}_{-0.20}$	$0.25^{+0.04}_{-0.07}$

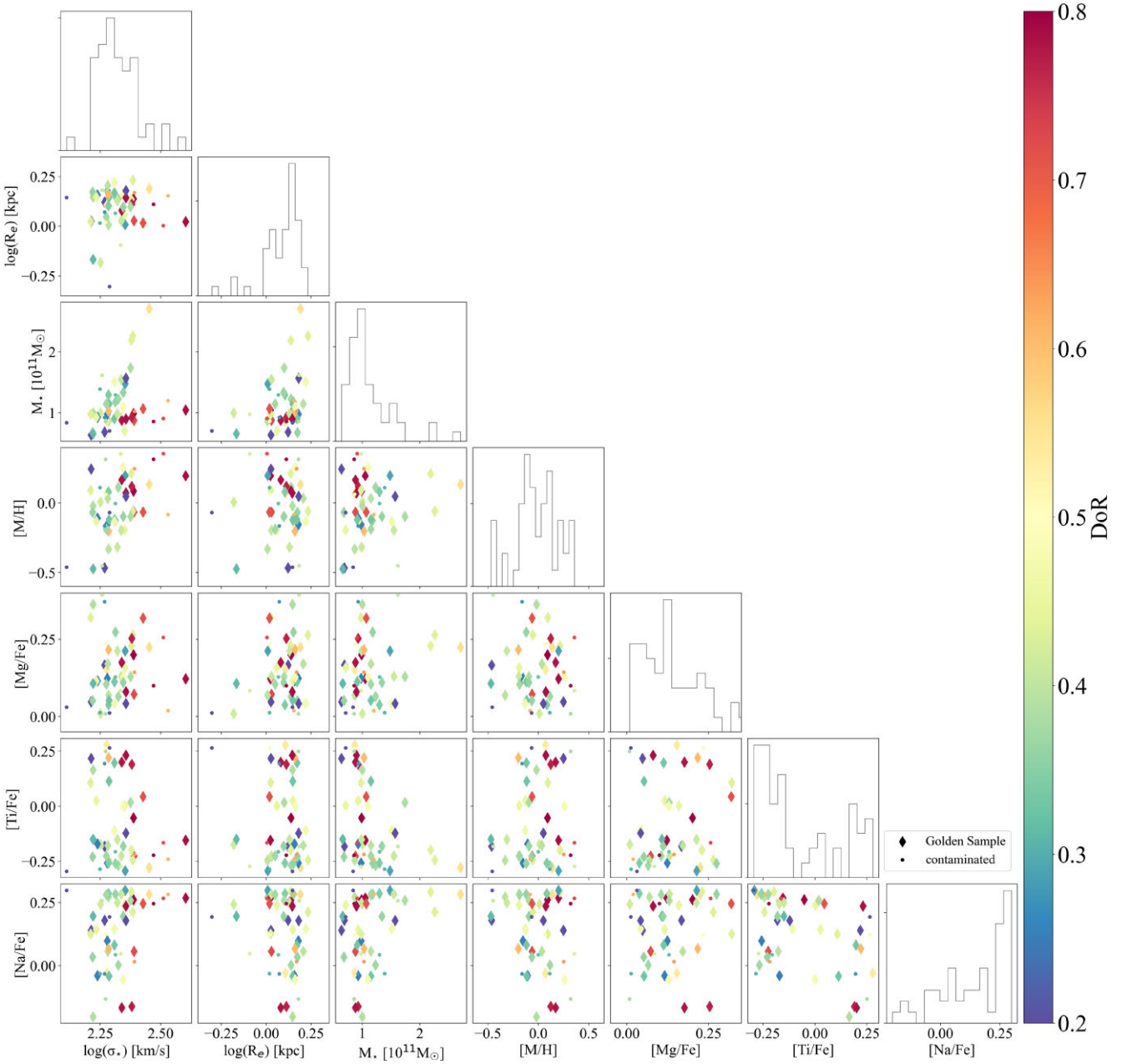

Figure 3. Stellar population analysis results. The data points are colour-coded by the DoR, computed in DR3. The only two parameters that show a correlation with it are the stellar metallicity and stellar velocity dispersion, which are both larger for relics than for non-relics. Moreover, the most extreme relics (red points) seem to cluster around $\log(R_e) \sim 0$ kpc and $M_\star \sim 1$–1.5×10^{11} $M_\odot$.

3.1 Correlation between the stellar velocity dispersion and the DoR

As already mentioned in previous INSPIRE papers and at the beginning of Section 3, there is a clear correlation between the DoR and stellar velocity dispersion, which can be seen in Fig. 4. The points here are colour-coded by the number of bins, defined in Section 2.4 to assess the validity of the SSP assumption. To find the linear fit to the data, we used the LTSFIT PYTHON package, which implements the methods described in Section 3.2 of Cappellari et al. (2013a) and uses the least trimmed squares (LTS) technique to iteratively clip outliers. In this work however, since the sample is small, we have set a very high clipping threshold (10σ) so that none of the galaxies are clipped. Using the package, we draw the correlation for all galaxies (solid grey line), and only for those in the *Golden Sample* (dashed grey line). We then compute, for each of the two fits, the Pearson coefficient and its p-value to assess the statistical significance and we report them in Table 3. For both the *Golden Sample* and all galaxies, the correlation is strong (with Pearson correlation coefficient $r = 0.64$ for all galaxies and $r = 0.56$ for the *Golden Sample*) and statistically significant (with p-value $\ll 0.0005$ in both cases). Instead, restricting to only the most extreme cases, galaxies in the *Golden Sample* with $\text{sum}_5 > 0.95$, any meaningful relation is lost (p-value $\gg 0.05$). This might be due to the fact that the parameter space is too small to see any relation or to the fact that they all have very similar, high-velocity

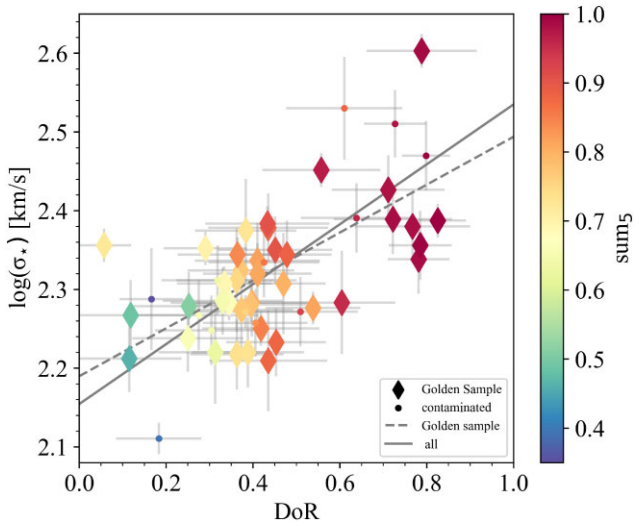

Figure 4. The stellar velocity dispersion against the DoR, colour-coded by the maximum sum of weights of five neighbouring bins of the age-distribution, quantifying how good the single-stellar population assumption is. Diamonds represent galaxies from the *Golden Sample*, while dots show the galaxies with contaminated spectral indices. The lines represent the linear fits for all of the galaxies (solid line) and the *Golden Sample* (dashed line).

Table 3. Linear fits to the stellar velocity dispersion versus the DoR (Fig. 4) for different sub-samples of galaxies. The last two columns report the Pearson correlation coefficient (r) and its p-value.

Sample	Linear fit	r	p
All	$\log(\sigma_\star) = [0.38 \times \mathrm{DoR}] + 2.16$	0.64	0.0000003
Golden Sample	$\log(\sigma_\star) = [0.30 \times \mathrm{DoR}] + 2.19$	0.56	0.00022

dispersion values, except for one system, J0909+0147 that will be the focus of a dedicated future publication.

For the INSPIRE objects, galaxies with higher DoR have a larger stellar velocity dispersion, which means that relics have a larger total mass with respect to non-relics. Since the stellar mass is comparable for all UCMGs in the sample, this might indicate a more concentrated and massive dark matter haloes or a dwarf-rich IMF, since dwarf stars contribute substantially to the mass but only add a few per cent to the optical light (Conroy 2013). Recent evidence seems to point towards the latter scenario, as no trace of dark matter has been found in NGC 1277, the most extreme relic in the local Universe (Comerón et al. 2023). However, a big caveat must be raised here: the Γ_b that we measure from the MILES models is the high-mass end of the IMF. Although steepening the slope at the high-mass end of the IMF effectively means increasing the dwarf-to-giant ratio, this is not fully equivalent to say that the number of dwarf stars is larger.

3.2 Correlation between stellar metallicity and DoR

In Fig. 5, we show the correlation between [M/H] and the DoR, colour-coding the data points by sum_5, as in the previous case. Once again, we fit a line to the points with the LTS technique, for all galaxies (solid), only these in the *Golden Sample* (dashed) and the non-contaminated ones with $\mathrm{sum}_5 > 0.95$ (dark red, dashed). The Pearson correlation coefficients and p-values for the three cases are listed in Table 4.

In this case, a weaker but still significant correlation is found. A large spread in metallicity is observed for objects with low and

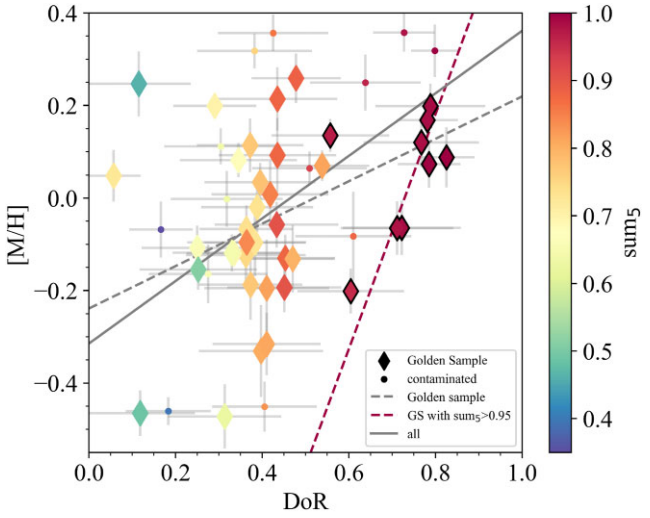

Figure 5. FIF fitted metallicity against the DoR, colour-coded by the maximum sum of weights of five neighbouring bins of the age-distribution. Symbols are as in previous figures. Here, *Golden Sample* galaxies with $\mathrm{sum}_5 > 0.95$ are marked by dark border. The lines represent the linear fits for the three samples, as indicated by the legend and listed in Table 4.

Table 4. Linear fits to the metallicity versus the DoR (Fig. 5) for different sub-samples of galaxies. The last two columns report the Pearson correlation coefficient (r) and its p-value.

Sample	Linear fit	r	p
All	$[\mathrm{M/H}] = [0.68 \times \mathrm{DoR}] - 0.315$	0.38	0.005
Golden Sample	$[\mathrm{M/H}] = [0.46 \times \mathrm{DoR}] - 0.24$	0.3	0.061
GS with $\mathrm{sum}_5 > 0.95$	$[\mathrm{M/H}] = [2.5 \times \mathrm{DoR}] - 1.8$	0.44	0.24

intermediate DoR, which also corresponds to a larger number of different ages that PPXF uses for the fit. For objects that pass the threshold having $\mathrm{sum}_5 > 0.95$, hence these for which the totality of the mass was formed during the first phase of the formation scenario, the scatter is reduced. A much steeper correlation between the DoR and [M/H] is found in this case, which is however statistically insignificant ($p > 0.05$). Nevertheless, the p-value drops down to 0.0036, and hence the relation is much more solid, when the outlying galaxy (J0224−3143, with DoR $\sim$ 0.5 and [M/H] $\sim$ 0.15) is not involved in the fitting.

3.3 Correlation between the IMF slope and the DoR

In this section, we focus on the stellar IMF and the correlation between its slope and the DoR, which is shown in Fig. 6. Although with a non-negligible scatter, objects with a higher DoR are better fitted with a steeper IMF slope. Also in this case, we apply the LTS fitting technique to the data and report the results in Table 5 for all galaxies, only these in the *Golden Sample* and only the most extreme ones with $\mathrm{sum}_5 > 0.95$. A statistically significant correlation is found for all the considered samples.

All the extreme relics, i.e. DoR > 0.7, are inconsistent with having a Milky Way IMF and require a steeper slope. However, we note that there are objects with a DoR as low as ∼0.3 (i.e. non-relics) that fit with an IMF slope equally steep than objects with a higher DoR.

This result is fully consistent with the results in INSPIRE – IV in which we found a larger scatter in the IMF slope of non-relics than that of relics, which might be caused by the fact

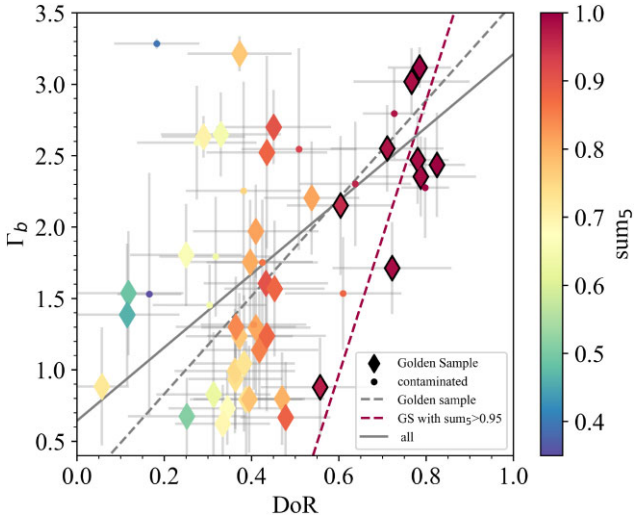

Figure 6. The slope of the IMF against the DoR, colour-coded by the maximum sum of weights of five neighbouring bins of the age-distribution. Symbols and lines are as in previous figures. The relations and their statistical significance are reported in Table 5.

Table 5. Linear fits to the IMF slope versus the DoR (Fig. 6) for different sub-samples of galaxies. The last two columns report the Pearson correlation coefficient (r) and its p-value.

Sample	Linear fit	r	p
All	$\Gamma_b = [2.57 \times \mathrm{DoR}] + 0.64$	0.4	0.0033
Golden Sample	$\Gamma_b = [3.42 \times \mathrm{DoR}] + 0.15$	0.5	0.0012
GS with $\mathrm{sum}_5 > 0.95$	$\Gamma_b = [9.6 \times \mathrm{DoR}] - 4.8$	0.73	0.024

that the SSP assumption does not hold well for galaxies with a more extended SFH, that could have stellar populations with different IMFs (and age and [M/H]). Furthermore, it is important to stress that data and modelling systematics might play a role, increasing the scatter. Indeed, although we carefully checked each individual spectrum, we are aware that the SNR is, in some cases, towards the lower limit for which FIF produces trustable results.

To better understand why some galaxies with a relatively low DoR have a bottom-heavy IMF, we have considered each of the three addenda that went into the definition of the DoR (from INSPIRE DR3) separately. We remind the readers that the DoR is defined as the average of the fraction of stellar mass assembled at $z = 2$ (i.e. $f_{M^\star_{t\mathrm{BB}=3}}$), the inverse of the cosmic time at which 75 per cent of the stellar mass was in place (t_{75}), and the inverse of the final formation time (i.e. the time at which a galaxy has formed the 100 per cent of its stellar mass), rescaled to the age of the Universe at the redshift of each galaxy ($[t_{\mathrm{uni}} - t_{\mathrm{fin}}]/t_{\mathrm{uni}}$). The relation between the IMF slope and each of these three quantities is plotted in Fig. 7, with the same symbology used in other figures. Interestingly, the strongest relation is found with the $f_{M^\star_{t\mathrm{BB}=3}}$: there are no points with $\Gamma_b > 2$ for $f_{M^\star_{t\mathrm{BB}=3}} < 0.6$. Hence, UCMGs have a dwarf-rich IMF only when they have formed at least 60 per cent of their stellar mass at $z > 2$.

Moreover, there is a clear dependency of the IMF slope from the cosmic assembly time (second-left panel of Fig. 7), especially for objects with a very peaked SFH and very old ages.[9] The IMF is dwarf-richer than the Milky Way one for stellar populations formed at $z > 2$, i.e. during the first phase of the two-phase formation scenario. Finally, the third panel of the figure shows that the IMF tends to be bottom-heavy when $[t_{\mathrm{uni}} - t_{\mathrm{fin}}]/t_{\mathrm{uni}}$ is larger, i.e. when the galaxy stopped forming stars (even in very low percentage) earlier in time.

3.4 Correlation between the IMF slope and other parameters

Two of the most accredited relations involving global IMF variation are the IMF slope-velocity dispersion (Cappellari et al. 2012, 2013b; Ferreras et al. 2013; La Barbera et al. 2013; Spiniello et al. 2014) and the IMF–metallicity relation (Martín-Navarro et al. 2015c). In Fig. 8, we check whether we are able to reproduce them with the INSPIRE UCMGs.

The linear relation we found between the IMF slope and the stellar velociy dispersion is similar, but slightly steeper than that found from the literature on normal-sized ETGs covering a similar range in $\sigma_\star$ (La Barbera et al. 2013, magenta line, and Spiniello et al. 2014, cyan line). However, the correlation is almost insignificant from a statistical point of view both for only galaxies in the *Golden Sample* (p-value = 0.043), as well as for all the galaxies (with an even higher p-value of 0.18), as shown by the least-square fitting to the data (grey lines) in the left panel of Fig. 8 and reported in the upper block of Table 6. Indeed, we note that for the same value of $\sigma_\star$, we find a very large range of IMF slopes, hence making the linear relation statistically insignificant. We stress that objects with a higher DoR (redder colours) have systematically steeper IMF slopes.

The correlation between the IMF slope and the [M/H], also statistically insignificant (Table 6, lower block) is instead much weaker than the one reported in Martín-Navarro et al. (2015c). Furthermore, also in this case, we note that at equal metallicity, galaxies with a higher DoR have a dwarf-richer IMF.

Hence, we conclude that even though global relations have been reported (La Barbera et al. 2013; McDermid et al. 2014; Spiniello et al. 2014; Martín-Navarro et al. 2015c), which apparently seem to hold also for UCMGs, there might not be a casual connection between the IMF slope and the stellar velocity dispersion and metallicity. Or, at least, these two factors are not the only drivers of the variations in the slope of the IMF. Hints from the fact that the local value of the stellar velocity dispersion is not the main driver behind dwarf-to-giant ratio variations was already suggested by Martín-Navarro et al. (2015b) for the local relic NGC 1277.

We speculate that the relations might arise from the fact that by selecting a galaxy with a larger velocity dispersion (i.e. a more massive galaxy), or with a metal richer population, the chances to find a compact progenitor in its centre (or a relic) are higher (Pulsoni et al. 2021). In this case, the excess in the dwarf-to-giant ratio might be restricted only to the central region, where the relic dominates the light. This is for instance the case of NGC 3311, the central galaxy of the Hydra-I cluster. From very high-SNR spatially resolved spectra, Barbosa et al. (2021b) found a bottom-heavy IMF slope in the galaxy's centre, where the stellar velocity dispersion was as low as ∼150 km s^{-1}. In this region, the stars are extremely old and metal-rich. The IMF becomes instead Milky Way-like moving away from the centre, where the $\sigma_\star$ rises up to ∼400 km s^{-1}, and both age and metallicity drop.

[9]The only exception is J0224−3143, with DoR = 0.56, $\mathrm{sum}_5 > 0.95$ but Γ_b as low as 0.88.

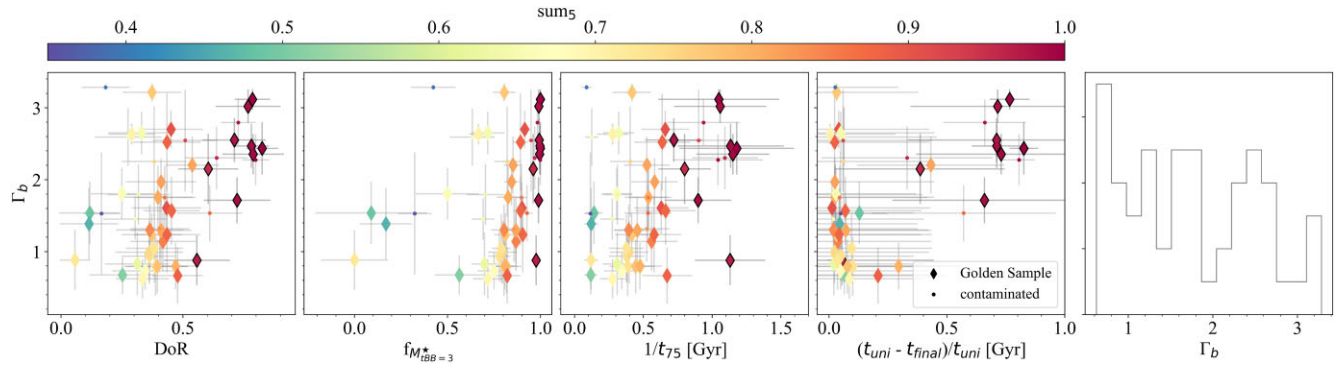

Figure 7. The slope of the IMF against the DoR (left) and the three quantities that were used to define it, and the distribution of Γ_b inferred for the 52 UCMGs (histogram in the right-most panel). The data points are colour-coded by the maximum sum of weights help by five neighbouring bins of the age-distribution. Diamonds represent galaxies from the *Golden Sample*, while dots mark the galaxies with contaminated spectral indices.

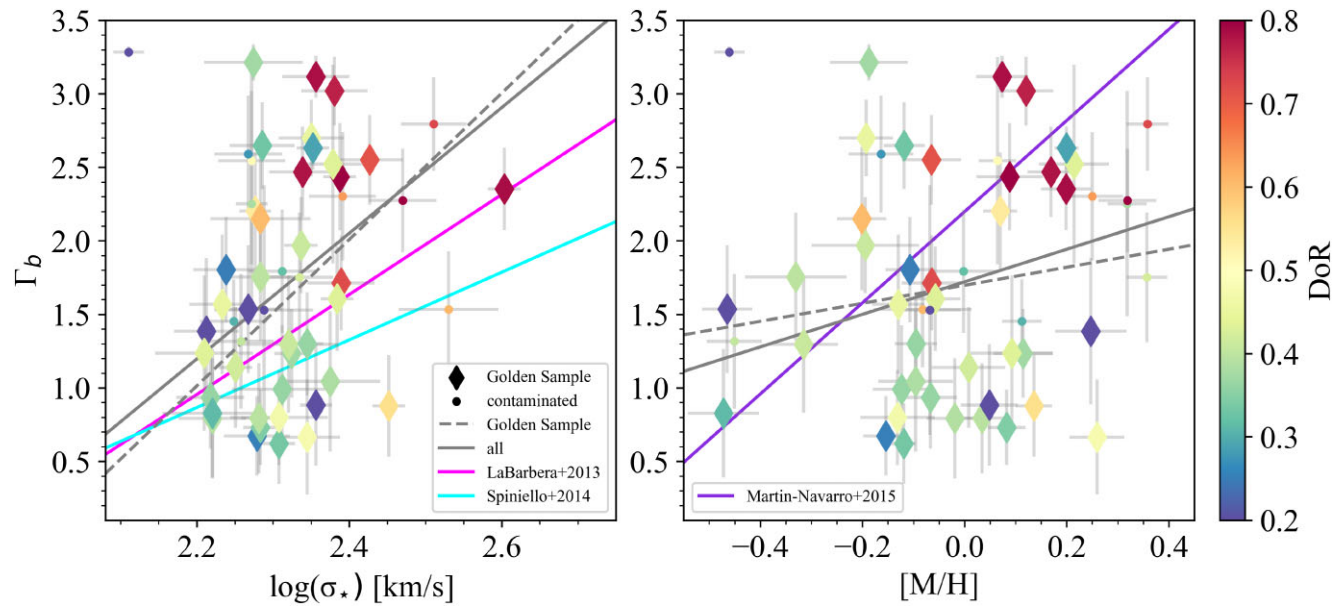

Figure 8. Stellar IMF slope versus stellar velocity dispersion (left, computed in DR3) and total stellar metallicity (right, computed with FIF). The INSPIRE galaxies are colour-coded by their DoR (top row) and sum_5 (bottom row). The lines show linear fits to the data, from this work (grey) and from literature papers, as reported in the legend and in the third and fourth block of Table 6. Symbols are like in other figures.

Table 6. Linear fits to the IMF slope versus the stellar velocity dispersion (first block) and the metallicity (second block) for different sub-samples of galaxies (Fig. 8). The last two columns report the Pearson correlation coefficient (r) and its p-value.

Sample	Linear fit	r	p
All	$\Gamma_b = [4.3 \times \log(\sigma_\star)] - 8.2$	0.19	0.18
Golden Sample	$\Gamma_b = [5 \times \log(\sigma_\star)] - 9.9$	0.33	0.043
All	$\Gamma_b = [1.11 \times [\mathrm{M/H}]] + 1.72$	0.13	0.35
Golden Sample	$\Gamma_b = [0.61 \times [\mathrm{M/H}]] + 1.7$	0.12	0.45

4 DISCUSSION

The results presented in this paper unambiguously demonstrate that a correlation exists between the IMF slope, the stellar velocity dispersion, the stellar metallicity, and the cosmic epoch of star formation for UCMGs. In particular, we found that, among the 52 INSPIRE UCMGs, the objects with the highest DoR, i.e. those that formed the totality of their stellar masses at $z > 2$ and did not experience any other star formation episode, i.e. extreme relics, are metal richer and have a dwarf-rich IMF.

This result could seem in strong disagreement with the latest findings from *JWST* data, suggesting that the IMF might be top-heavy, i.e. giant richer, at very high redshift (Cameron et al. 2023; Trinca et al. 2023; Woodrum et al. 2023). However, we note that, in principle, the high- and low-mass ends of the IMF are not necessarily coupled, as already highlighted by Fontanot et al. (2018). In particular, incorporating explicitly the effects of cosmic rays as regulators of the chemical and thermal state of the gas in the dense cores of molecular clouds, they conclude that the IMF slope could possibly be simultaneously shallower at high-mass end and steeper at the low-mass end than a Kroupa IMF.

Here below, we highlight a couple of possible scenarios that would allow us to reconcile the different observations.

In the context of the integrated galaxy-wide stellar initial mass functions (IGIMFs) paradigm (Kroupa 1995; Kroupa & Weidner 2003), all stars form in groups or embedded star clusters, and the most massive star that can be formed in them depends on the mass

and the metallicity of the star cluster (Weidner, Kroupa & Bonnell 2010; Dabringhausen & Kroupa 2023). The IGIMF will then be the combination of all the stars that formed in the different star clusters of a galaxy (Kroupa & Weidner 2003). Furthermore, recent simulations on the first, metal-free stars suggest that the fraction of massive stars directly depends on the gas temperature of star-forming clouds: the higher the temperature the larger the mass of the produced stars (Abel, Bryan & Norman 2002; Fukushima et al. 2020). Also, the top-heaviness of the IMF depends on the metallicity of the gas (the lower the metallicity the more top-heavy the IMF would be; Fukushima et al. 2020) and on the background radiation intensity (the higher the intensity the more top-heavy the IMF would be; Chon et al. 2022). Hence, one possibility is that the IMF could be top-heavy in low-metallicity and dense gas environments (Dabringhausen et al. 2012; Dib 2023) while it becomes progressively bottom-heavy as the metallicity of the environment increases (Chabrier et al. 2014), at any redshifts. However, we do not find a strong dependency of the low-mass end of the IMF on the measured stellar metallicity. Moreover, from a theoretical point of view these scenarios are still very debated. For instance, opposite to what was just described, Bate (2023) suggested, from three radiation hydrodynamical simulations of star cluster formation with different metallicities that the IMF is M-dwarfs deficient (i.e. bottom-light) in high-metallicity star formation at early epochs ($z \geq 5$).

Another interesting possibility, perhaps able to reconcile these contrasting results, is to allow for a time-evolution of the IMF slope (Vazdekis et al. 1996, 1997; Weidner et al. 2013; Ferreras et al. 2015). A first and quick phase with a top-heavy IMF occurs at a very high-redshift ($z \geq 5$). Then, the very massive ($M > 50$ M$_\odot$) giant stars rapidly die (less than 10 Myr; Yusof et al. 2013), polluting the interstellar medium with metals. At this point, if the conditions of the local environment (i.e. gas temperature, pressure, and density) are extreme, and a violent starburst happens, fragmentation of the star formation clouds becomes easier (Chabrier et al. 2014) and therefore a large number of dwarf stars are produced, transforming the IMF into a bottom-heavy one. In fact, according to theoretical works (e.g. Hennebelle & Chabrier 2008), a larger fraction of low-mass cores in very dense, hot, and highly turbulent environments is a direct consequence of the enhanced gas compression by highly turbulent motions and of the shorter free–fall times for the collapsing overdense region (Chabrier et al. 2014). This scenario, also naturally explains why relics are metal-richer than non-relics, as they formed in a metal-rich gas. Finally, stars are produced following a canonical Milky Way-like IMF slope for the more time-extended standard star formation occurring during the second phase of the two-phase formation scenario.

5 CONCLUSIONS

In this paper, the sixth of the INSPIRE (Spiniello et al. 2021a, b) series, we have presented an extensive stellar populations analysis on the entire INSPIRE sample made of 52 ultra-compact ($R_e < 2$ kpc) massive ($M_\star > 6 \times 10^{10}$ M$_\odot$) galaxies (UCMGs) at $0.1 < z < 0.4$. Of these, 38 were confirmed as relics in INSPIRE DR3, as they formed more than 75 per cent of their stellar mass by the end of the first phase of the formation scenario. At the time of writing, this is the largest catalogue of spectroscopically confirmed relics known in the nearby Universe.

In INSPIRE DR3 the stellar population ages and metallicities were inferred fitting UVB + VIS spectra, joined and convolved to a common final resolution of FWHM = 2.51 Å, in the wavelength range [3500–7000] Å. The [Mg/Fe] abundances were instead obtained directly from line index analysis, with the Mg$_b$–Fe24 index–index plot. The IMF slope was kept fixed to a Kroupa-like one with $\Gamma_b = 1.3$ and all other elemental abundances were assumed to be solar. Here, instead, we have used the FIF technique to infer stellar metallicities, [Mg/Fe], [Ti/Fe], and [Na/Fe] ratios, and IMF slope from the same spectra. This much more flexible approach, combined with a careful visual inspection of each single spectrum, allowed us to investigate whether a correlation exists between the stellar population parameters and the DoR. We have been also able, for the first time, to infer the low-mass end of the IMF slope of individual UCMGs outside the local Universe. Moreover, we have tested for which systems the SSP assumption holds, by quantifying the spread in age between all the stellar models used by the PPXF fit and assesses whether the derived relation depends upon this quantity.

In particular, we found:

(i) a clear correlation between the velocity dispersion and the DoR, confirming the results already presented in previous INSPIRE papers: at equal stellar mass relics have larger $\sigma_\star$ than non-relics (Fig. 4);

(ii) a linear relation between the stellar metallicity and the DoR, although with a large scatter (Fig. 5). The slope of the relation is much steeper considering only extreme relics for which the SSP assumption certainly holds but it becomes statistically not significant in this case (p-value = 0.24). We note however that this might be caused by the single outlier J0224−3143, with DoR = 0.56 and [M/H] = 0.14;

(iii) a correlation between the IMF slope and the DoR, with a scatter that increases when the stellar population fit requires a larger number of SSP models with different ages. Specifically, all UCMGs with DoR > 0.7, i.e. extreme relics, require an IMF with a dwarf-to-giant ratio larger than that of the Milky Way, with slopes of $\Gamma_b \geq 1.8$. For UCMGs with lower DoR, the spread in the IMF slope becomes very large, consistent with what was found in INSPIRE – IV (Fig. 6);

(iv) considering the three components forming the DoR, the IMF slope correlates strongly with the inverse of the time at which 75 per cent of the stellar mass was formed. Moreover, there are no UCMGs with $\Gamma_b > 2$ when the fraction of stellar mass formed by $z \sim 2$ is lower than 60 per cent and no objects with $\Gamma_b < 1.7$ when $[t_{\rm uni} - t_{\rm fin}]/t_{\rm uni} > 0.6$, i.e. when the mass assembly has ended early on in cosmic time (Fig. 7);

(v) no statistically significant correlation between the slope of the IMF and the stellar velocity dispersion and between the slope of the IMF and the stellar metallicity (Fig. 8). The former (latter) seems to be steeper (shallower) than the ones obtained in the literature for normal-sized ETGs. From the colour-coding of the points in Fig. 8, it appears that at equal velocity dispersion and/or metallicity, galaxies with a higher DoR have a bottom-heavy IMF.

In conclusion, our data support a scenario whereby an excess of dwarf-to-giant ratio might originate from the first phase of the mass assembly at high-z when the density and temperature of the Universe were higher, and thus when fragmentation might have been easier (Chabrier et al. 2014). However, to reconcile the very recent findings at very high-z from *JWST* (e.g. Cameron et al. 2023), as well as high-resolution simulations (e.g. Bate 2023), we speculate that the IMF might vary with cosmic time (Vazdekis et al. 1996, 1997; Weidner et al. 2013; Ferreras et al. 2015). An incredibly quick top-heavy phase at very high-z (>5), that produces very metal-poor stars of ∼100 M$_\odot$. These stars quickly die and pollute the interstellar medium with metals. Then, a large number of dwarfs is produced in regions of high density and temperature, through fast starbursts up to $z \sim 2$, while stars are distributed with a Milky Way-like IMF slope if they formed in the second phase of the two-phase formation scenario, under less extreme temperature and density conditions.

ACKNOWLEDGEMENTS

The authors are thankful to Prof. Vazdekis for interesting discussions that improved the quality of the paper. CS, CT, DB, and PS acknowledge funding from the PRIN-INAF 2020 programme 1.05.01.85.11. AFM acknowledges support from RYC2021-031099-I and PID2021-123313NA-I00 of MICIN/AEI/10.13039/501100011033/FEDER, UE, NextGenerationEU/PRT. DS was supported by JPL, which is operated under a contract by Caltech for NASA. GD acknowledges support by UKRI-STFC grants: ST/T003081/1 and ST/X001857/1.

DATA AVAILABILITY

The data described in this paper are publicly available via the ESO Phase 3 Archive Science Portal under the collection `INSPIRE` (https://archive.eso.org/scienceportal/home?data_collection = INSPIRE, https://doi.eso.org/10.18727/archive/36).

REFERENCES

Abel T., Bryan G. L., Norman M. L., 2002, Science, 295, 93
Barbosa C. E., Spiniello C., Arnaboldi M., Coccato L., Hilker M., Richtler T., 2021a, A&A, 645, L1
Barbosa C. E., Spiniello C., Arnaboldi M., Coccato L., Hilker M., Richtler T., 2021b, A&A, 649, A93
Bate M. R., 2023, MNRAS, 519, 688
Bennett C. L., Larson D., Weiland J. L., Hinshaw G., 2014, ApJ, 794, 135
Blumenthal G. R., Faber S. M., Primack J. R., Rees M. J., 1984, Nature, 311, 517
Buitrago F. et al., 2018, A&A, 619, A137
Cameron A. J., Katz H., Witten C., Saxena A., Laporte N., Bunker A. J., 2023, preprint (arXiv:2311.02051)
Cappellari M., 2017, MNRAS, 466, 798
Cappellari M., 2023, MNRAS, 526, 3273
Cappellari M., Emsellem E., 2004, PASP, 116, 138
Cappellari M. et al., 2012, Nature, 484, 485
Cappellari M. et al., 2013a, MNRAS, 432, 1709
Cappellari M. et al., 2013b, MNRAS, 432, 1862
Chabrier G., Hennebelle P., Charlot S., 2014, ApJ, 796, 75
Charbonnier A. et al., 2017, MNRAS, 469, 4523
Chon S., Ono H., Omukai K., Schneider R., 2022, MNRAS, 514, 4639
Comerón S. et al., 2023, A&A, 675, A143
Conroy C., 2013, ARA&A, 51, 393
Conroy C., van Dokkum P., 2012a, ApJ, 747, 69
Conroy C., van Dokkum P. G., 2012b, ApJ, 760, 71
D'Ago G. et al., 2023, A&A, 672, A17, INSPIRE DR2
Dabringhausen J., Kroupa P., 2023, MNRAS, 526, 2301
Dabringhausen J., Kroupa P., Pflamm-Altenburg J., Mieske S., 2012, ApJ, 747, 72
Damjanov I., Chilingarian I., Hwang H. S., Geller M. J., 2013, ApJ, 775, L48
Damjanov I., Hwang H. S., Geller M. J., Chilingarian I., 2014, ApJ, 793, 39
Damjanov I., Geller M. J., Zahid H. J., Hwang H. S., 2015, ApJ, 806, 158
Dib S., 2023, ApJ, 959, 88
Eappen R., Kroupa P., 2024, MNRAS, 528, 4264
Eftekhari E., La Barbera F., Vazdekis A., Allende Prieto C., Knowles A. T., 2022, MNRAS, 512, 378
Falcón-Barroso J., Sánchez-Blázquez P., Vazdekis A., Ricciardelli E., Cardiel N., Cenarro A. J., Gorgas J., Peletier R. F., 2011, A&A, 532, A95
Ferré-Mateu A., Mezcua M., Trujillo I., Balcells M., van den Bosch R. C. E., 2015, ApJ, 808, 79
Ferré-Mateu A., Trujillo I., Martín-Navarro I., Vazdekis A., Mezcua M., Balcells M., Domínguez L., 2017, MNRAS, 467, 1929
Ferreras I., La Barbera F., de la Rosa I. G., Vazdekis A., de Carvalho R. R., Falcón-Barroso J., Ricciardelli E., 2013, MNRAS, 429, L15
Ferreras I., Weidner C., Vazdekis A., La Barbera F., 2015, MNRAS, 448, L82
Flores-Freitas R., Chies-Santos A. L., Furlanetto C., De Rossi M. E., Ferreira L., Zenocratti L. J., Alamo-Martínez K. A., 2022, MNRAS, 512, 245
Fontanot F., La Barbera F., De Lucia G., Pasquali A., Vazdekis A., 2018, MNRAS, 479, 5678
Fukushima H., Hosokawa T., Chiaki G., Omukai K., Yoshida N., Kuiper R., 2020, MNRAS, 497, 829
Hennebelle P., Chabrier G., 2008, ApJ, 684, 395
Kroupa P., 1995, MNRAS, 277, 1522
Kroupa P., Weidner C., 2003, ApJ, 598, 1076
La Barbera F., de Carvalho R. R., Kohl-Moreira J. L., Gal R. R., Soares-Santos M., Capaccioli M., Santos R., Sant'anna N., 2008, PASP, 120, 681
La Barbera F., Ferreras I., Vazdekis A., de la Rosa I. G., de Carvalho R. R., Trevisan M., Falcón-Barroso J., Ricciardelli E., 2013, MNRAS, 433, 3017
La Barbera F., Vazdekis A., Ferreras I., Pasquali A., Allende Prieto C., Röck B., Aguado D. S., Peletier R. F., 2017, MNRAS, 464, 3597
La Barbera F. et al., 2019, MNRAS, 489, 4090
Lisiecki K., Małek K., Siudek M., Pollo A., Krywult J., Karska A., Junais, 2023, A&A, 669, A95
Lohmann F. S., Schnorr-Müller A., Trevisan M., Ricci T. V., Clerici K. S., 2023, MNRAS, 524, 5266
Martín-Navarro I., Barbera F. L., Vazdekis A., Falcón-Barroso J., Ferreras I., 2015a, MNRAS, 447, 1033
Martín-Navarro I., La Barbera F., Vazdekis A., Ferré-Mateu A., Trujillo I., Beasley M. A., 2015b, MNRAS, 451, 1081
Martín-Navarro I. et al., 2015c, ApJ, 806, L31
Martín-Navarro I., van de Ven G., Yıldırım A., 2019, MNRAS, 487, 4939
Martín-Navarro I. et al., 2021, A&A, 654, A59
Martín-Navarro I. et al., 2023, MNRAS, 521, 1408
McDermid R. M. et al., 2014, ApJ, 792, L37
Moura M. T., Chies-Santos A. L., Furlanetto C., Zhu L., Canossa-Gosteinski M. A., 2024, MNRAS, 528, 353
Navarro-González J., Ricciardelli E., Quilis V., Vazdekis A., 2013, MNRAS, 436, 3507
Parikh T. et al., 2018, MNRAS, 477, 3954
Pietrinferni A., Cassisi S., Salaris M., Castelli F., 2004, ApJ, 612, 168
Pietrinferni A., Cassisi S., Salaris M., Castelli F., 2006, ApJ, 642, 797
Poggianti B. M., Moretti A., Calvi R., D'Onofrio M., Valentinuzzi T., Fritz J., Renzini A., 2013, ApJ, 777, 125
Pulsoni C., Gerhard O., Arnaboldi M., Pillepich A., Rodriguez-Gomez V., Nelson D., Hernquist L., Springel V., 2021, A&A, 647, A95
Renzini A., 2006, ARA&A, 44, 141
Salpeter E. E., 1955, ApJ, 121, 161
Salvador-Rusiñol N., Beasley M. A., Vazdekis A., Barbera F. L., 2021, MNRAS, 500, 3368
Sánchez-Blázquez P., Gorgas J., Cardiel N., 2006, A&A, 457, 823
Sarzi M., Spiniello C., La Barbera F., Krajnović D., van den Bosch R., 2018, MNRAS, 478, 4084
Saulder C., van den Bosch R. C. E., Mieske S., 2015, A&A, 578, A134
Scognamiglio D. et al., 2020, ApJ, 893, 4
Shih H.-Y., Stockton A., 2011, ApJ, 733, 45
Siudek M. et al., 2023, MNRAS, 523, 4294
Smith R. J., 2020, ARA&A, 58, 577
Spiniello C., Trager S. C., Koopmans L. V. E., Chen Y. P., 2012, ApJ, 753, L32
Spiniello C., Trager S., Koopmans L. V. E., Conroy C., 2014, MNRAS, 438, 1483
Spiniello C., Napolitano N. R., Coccato L., Pota V., Romanowsky A. J., Tortora C., Covone G., Capaccioli M., 2015a, MNRAS, 452, 99
Spiniello C., Barnabè M., Koopmans L. V. E., Trager S. C., 2015b, MNRAS, 452, L21
Spiniello C., Trager S. C., Koopmans L. V. E., 2015c, ApJ, 803, 87
Spiniello C. et al., 2021a, A&A, 646, A28, INSPIRE Pilot
Spiniello C. et al., 2021b, A&A, 654, A136, INSPIRE DR1
Spiniello C. et al., 2023, MNRAS, 527, 8793

Taylor E. N., Franx M., Glazebrook K., Brinchmann J., van der Wel A., van Dokkum P. G., 2010, ApJ, 720, 723
Tortora C., Pipino A., D'Ercole A., Napolitano N. R., Matteucci F., 2013, MNRAS, 435, 786
Tortora C. et al., 2016, MNRAS, 457, 2845
Tortora C. et al., 2018, MNRAS, 481, 4728
Trager S. C., Worthey G., Faber S. M., Burstein D., González J. J., 1998, ApJS, 116, 1
Treu T., Auger M. W., Koopmans L. V. E., Gavazzi R., Marshall P. J., Bolton A. S., 2010, ApJ, 709, 1195
Trinca A., Schneider R., Valiante R., Graziani L., Ferrotti A., Omukai K., Chon S., 2023, MNRAS, 529, 3563
Trujillo I., Cenarro A. J., de Lorenzo-Cáceres A., Vazdekis A., de la Rosa I. G., Cava A., 2009, ApJ, 692, L118
Trujillo I., Carrasco E. R., Ferré-Mateu A., 2012, ApJ, 751, 45
Trujillo I., Ferré-Mateu A., Balcells M., Vazdekis A., Sánchez-Blázquez P., 2014, ApJ, 780, L20
Valentinuzzi T. et al., 2010, ApJ, 712, 226
van Dokkum P. G. et al., 2010, ApJ, 709, 1018
van Dokkum P., Conroy C., Villaume A., Brodie J., Romanowsky A. J., 2017, ApJ, 841, 68
Vazdekis A., Casuso E., Peletier R. F., Beckman J. E., 1996, ApJS, 106, 307
Vazdekis A., Peletier R. F., Beckman J. E., Casuso E., 1997, ApJS, 111, 203
Vazdekis A., Sánchez-Blázquez P., Falcón-Barroso J., Cenarro A. J., Beasley M. A., Cardiel N., Gorgas J., Peletier R. F., 2010, MNRAS, 404, 1639
Vazdekis A. et al., 2015, MNRAS, 449, 1177
Vernet J. et al., 2011, A&A, 536, A105
Weidner C., Kroupa P., Bonnell I. A. D., 2010, MNRAS, 401, 275
Weidner C., Ferreras I., Vazdekis A., La Barbera F., 2013, MNRAS, 435, 2274
Woodrum C. et al., 2023, preprint (arXiv:2310.18464)
Worthey G., 1994, ApJS, 95, 107
Yıldırım A., van den Bosch R. C. E., van de Ven G., Husemann B., Lyubenova M., Walsh J. L., Gebhardt K., Gültekin K., 2015, MNRAS, 452, 1792
Yıldırım A., van den Bosch R. C. E., van de Ven G., Martín-Navarro I., Walsh J. L., Husemann B., Gültekin K., Gebhardt K., 2017, MNRAS, 468, 4216
Yusof N. et al., 2013, MNRAS, 433, 1114
Zolotov A. et al., 2015, MNRAS, 450, 2327

APPENDIX A: GOLDEN SAMPLE SELECTION

In Section 2.3, we have selected six indices that have allowed us to infer the age, metallicity, [Mg/Fe], [Ti/Fe], [Na/Fe] abundances, and IMF slope. To assess which of these features were contaminated in each of the galaxies we have performed three different tests:

(i) we have visually inspected all the 52 spectra, flagging clear emission lines, and residuals contaminating the indices,
(ii) we have plotted the histogram distribution of the indices computed on all the models varying all the parameters, and have flagged systems for which a given index falls outside this distribution,
(iii) we have produced as many index–index plots as possible, creating large model grids with changing resolution (in km s^{-1}) and elemental abundance.

The result of this latter test is visualized in Fig. A1. Here, we show four representative index–index plots (top: Mg2 versus the two Fe lines, bottom: NaD versus the two TiO lines) and a series of grids predicted by the MILES SSP models. For each panel, if a galaxy falls outside the model grid, it is highlighted with a black cross and flagged as 'contaminated'. We note that we have performed these tests considering a larger set of indices but still arising from the same chemical elements (HβG, Hβ, Hβ0, Mg2, Mgb5117, Fe5015, Fe5270, Fe5335, Fe5709, NaD, HδA, TiO1, TiO2, TiO3). This was done in order to select, for each element the least-contaminated index.

Indeed, inspecting by eye each of the spectra, we found that for 39/52 UCMGs, the six indices mentioned above are clean from residual sky-lines and bad pixels. The final sample of 39 uncontaminated, old galaxies has thus been denoted as the *Golden Sample*. All the plots presented in the main body of this paper always show them as diamonds, while the objects for which one or more indices are contaminated are plotted as circles.

At this point, as a further test for the robustness of our results, we have made several modelling runs with different combinations of spectral indices and different setups (e.g. not fitting for [Na/Fe]

Table A1. FIF runs with different configurations. The first row reports our fiducial run, based on six indicators: Mgb, Fe5270, Fe5335, NaD, TiO1, and TiO2. The other 18 runs, have been used to test different assumptions, indices, and setups, as described in detail in the text.

Run	Hydrogen index	Magnesium index	Iron index	Titanium index	Sodium index	Notes	# of galaxies
Fiducial	–	Mgb5177	Fe5270, Fe5335	TiO1, TiO2	NaD		39
1	–	Mgb5177	Fe5270, Fe5335	TiO1, TiO2	–	Not fitting for [Na/Fe]	40
2	–	Mg2	Fe5270, Fe5335	TiO1, TiO2	NaD	Testing a different Mg index	39
3	–	Mgb5177	Fe5270, Fe5335	TiO1, TiO2	–		40
4	–	Mgb5177	Fe5270, Fe5335	TiO1, TiO2, TiO3	NaD	Testing more TiO lines	35
5	–	Mgb5177	Fe5015, Fe5270, Fe5335, Fe5709	TiO1, TiO2	NaD	Testing more Fe lines	31
6	–	Mgb2	Fe5015, Fe5270, Fe5335, Fe5709	TiO1, TiO2	NaD		31
7	H βG	Mgb5177	Fe5270, Fe5335	TiO1, TiO2	NaD	Age fixed	38
8	H βG	Mg2	Fe5270, Fe5335	TiO1, TiO2	NaD	Age fixed, different Mg index	38
9	H βG	Mg2	Fe5270, Fe5335	TiO1, TiO2	NaD	Age free to vary	38
10	H δA	Mg2	Fe5270, Fe5335	TiO1, TiO2	NaD	Testing a different age index	37
11	H δA	Mgb5177	Fe5270, Fe5335	TiO1, TiO2	NaD		37
12	H βG, H δA	Mgb5177	Fe5270, Fe5335	TiO1, TiO2	NaD		36
13	H βG, H δA	Mg2	Fe5270, Fe5335	TiO1, TiO2	NaD		36
14	H βG	Mgb5177	Fe5015, Fe5270, Fe5335, Fe5709	TiO1, TiO2	NaD	Adding more iron lines	29
15	H βG	Mg2	Fe5015, Fe5270, Fe5335, Fe5709	TiO1, TiO2	NaD		29
16	H δA	Mgb5177	Fe5015, Fe5270, Fe5335, Fe5709	TiO1, TiO2	NaD		30
17	H δA	Mg2	Fe5015, Fe5270, Fe5335, Fe5709	TiO1, TiO2	NaD		30
18	H βG, H δA	Mgb5177	Fe5015, Fe5270, Fe5335, Fe5709	TiO1, TiO2	NaD		28
19	H βG, H δA	Mg2	Fe5015, Fe5270, Fe5335, Fe5709	TiO1, TiO2	NaD		28

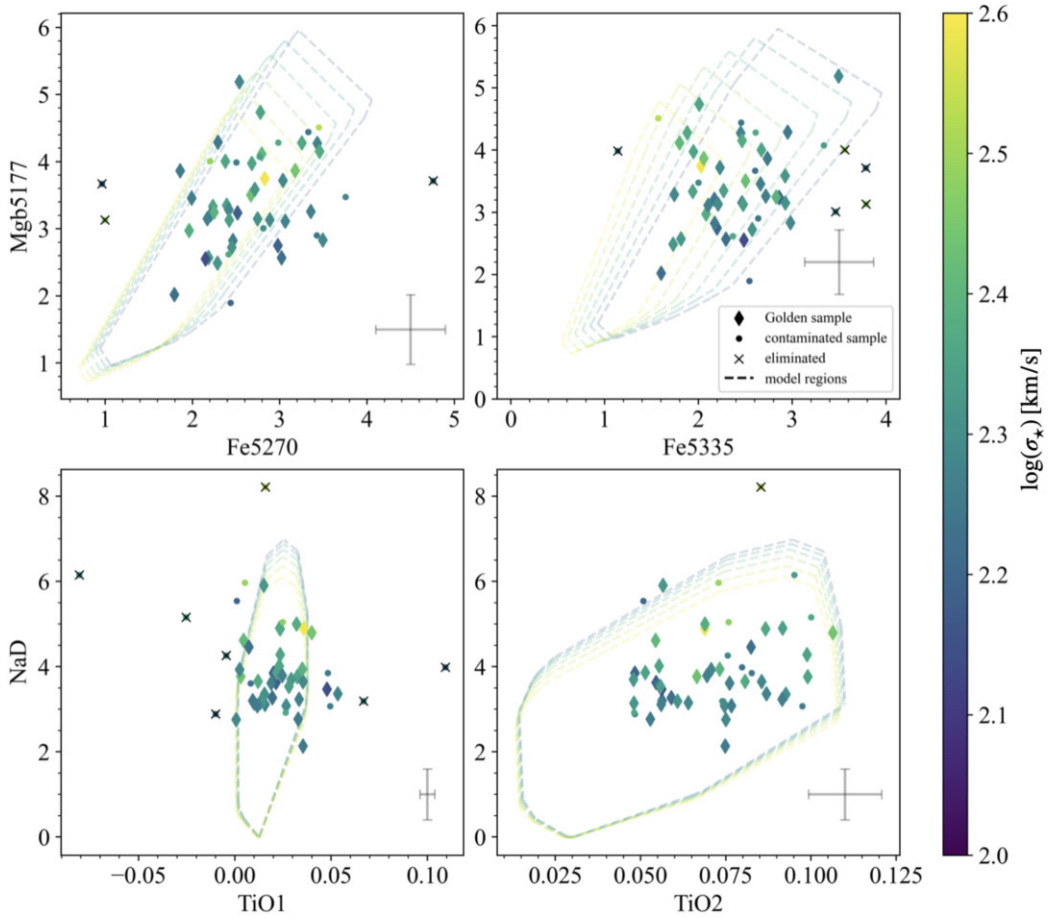

Figure A1. Examples of four index–index plots showing the SSP model grid and the measurements for the INSPIRE galaxies colour-coded by their resolution/velocity dispersion. Systems that have no contaminated indices (*Golden Sample*) are marked by crosses, while systems that have at least one contaminated index are marked by a dot. The black circles mark the systems that were eliminated on each panel based on the corresponding indices. A typical error-bar is reported in the bottom right corner of each panel.

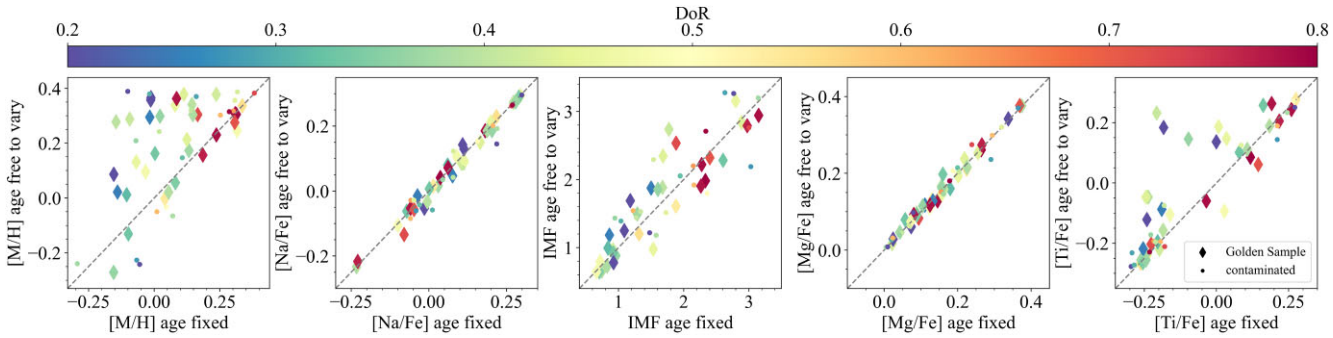

Figure A2. Comparison between the stellar population parameters obtained by keeping the age fixed to the one derived by PPXF and by letting the age free to vary. The data points are colour-coded by the DoR.

or/and not fixing for the age and hence including or not Balmer lines). All the runs are summarized in Table A1.

First (Runs 1–6), we investigated whether the results would differ greatly by excluding/including other spectral indices from the fiducial ones. In particular, in Runs 1 and 3 we have excluded the NaD index and not fitted for Na abundance, which did not lead to any notable changes in the modelled values. We note that we do not test the case without TiO indices and fixing the [Ti/Fe] to solar because the TiO indices are the best gravity-sensitive indicators and we need to include them in order to have a solid constraint on the IMF slope, which is the main goal of this paper. In Run 2, we have used an alternative definition of the Mgb spectral feature (Mg2 instead of the more classical Mgb5177, see Table C1 for the index definition), which led to larger metallicities at the cost of lower Na abundance, as seen in Fig. A3. These changes are systematic but are smaller for more extreme relics. Importantly, the IMF slopes inferred from the two runs are consistent within the errors, demonstrating that the inference on this parameter is robust.

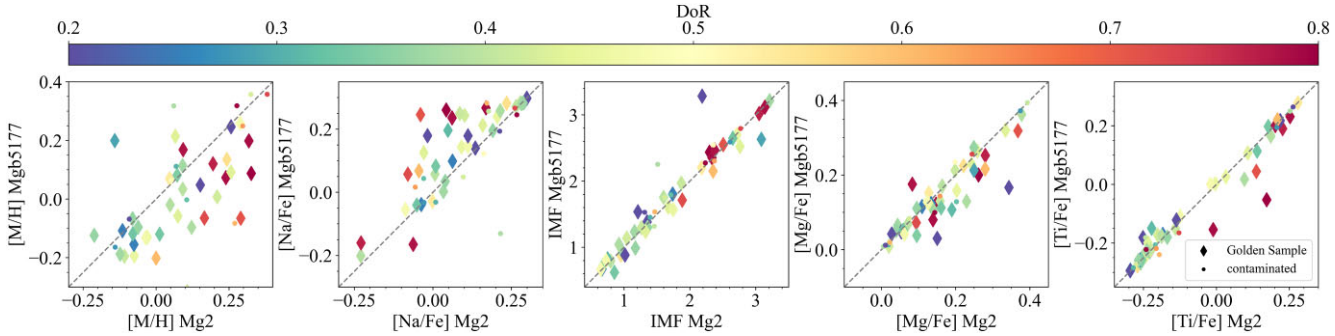

Figure A3. Comparison between the stellar population parameters obtained using the two different spectral index definitions for Magnesium (Mg2 and Mg5177). The data points are colour-coded by the DoR.

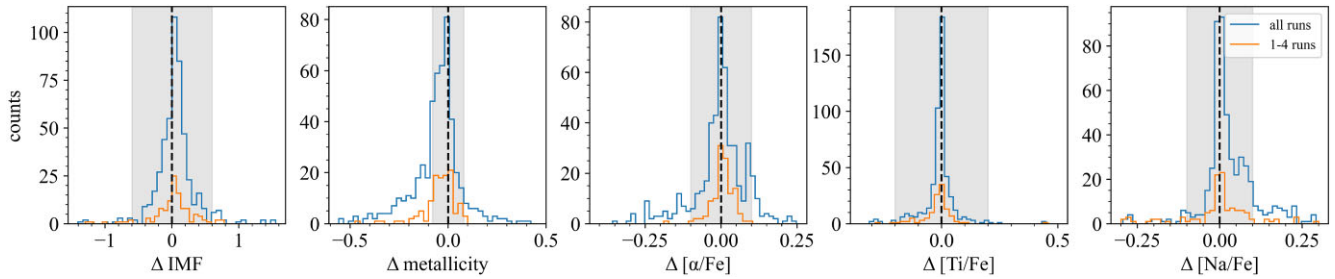

Figure A4. Histograms of the different results of all 19 FIF Runs (blue) and the Runs from 1 to 4 only (orange) and the fiducial fit. Each panel shows results for a different stellar population parameter. The majority of the results, as well as the overall distribution, is consistent with the fiducial fit results (within the errors, grey area), confirming the robustness of our fitting.

In Runs 4, 5, and 6, we have included more Ti and/or Fe spectral indices for both Mg indices), without significant changes to the results.

Secondly, for Runs 7–13, we focussed on the ages and investigated the impact of different age-sensitive features and methods. As already mentioned, for our fiducial fitting we have kept the age fixed to the one derived by PPXF and did not use any of the Balmer spectral indices. In Runs 7 and 8, we have tested the result of including $H\beta$ while keeping the age fixed. As expected, this did not lead to any significant changes in the inferred stellar population parameters (since hydrogen spectral indices mostly impact age). In Run 9, we have used the same set of indices as in the previous runs, but we have left the age free to vary from 0 to 14 Gyr. This led to significant changes in the resulting metallicities and Titanium abundances for low DoR objects, but not in the IMF slope and other chemical abundances, as can be seen in Fig. A2.

Finally, in the remaining runs, we have tested different combinations of the above-described changes to the fiducial set of indices. Remarkably, the inference on the IMF slope is very robust and does not change by changing the considered indices.

Considering also that the number of galaxies with uncontaminated indices is the greatest for the six chosen indices (see last column of Table 2), this is indeed the best choice.[10]

In Fig. A4, we show, for each galaxy in INSPIRE, the distribution of the difference between the value of each parameter inferred from the fiducial run and these inferred from the 19 different runs listed in Table A1. Each panel shows a stellar population parameter. The results of a great majority of the runs are consistent within the errors (grey vertical regions) with the fitting with the six chosen indices, which demonstrates that the results are robust and overall independent from the choice of the set of indicators.

[10]Removing NaD and not fitting for [Na/Fe] increases the number of galaxies by 1. However, it decreases the number of parameters constrained during the fit and might influence the inference on IMF (see Spiniello et al. 2014).

APPENDIX B: COMPARISON WITH INSPIRE DR3

In this Appendix, we compare the ages, metallicities, and velocity dispersion values, that we have obtained by fitting the SSP models with PPXF in the first step of the analysis presented in this paper, with the results published in INSPIRE DR3. We note however that a perfect agreement is not expected between these two measurements. We stress that, although the values are computed with the same code, the assumptions in the two cases were different. In fact, in INSPIRE DR3 we kept the IMF fix to $\Gamma_b = 1.3$ and performed the fit using models with a [α/Fe] value corresponding to the [Mg/Fe] ratio inferred from line indices. Here, we let the IMF vary during the fit but assume a solar α abundance for the models.

Moreover, the ages we presented in DR3, are averaged values obtained from the unregularized and the maximum regularized fit. Here, we do not perform any regularization. Finally, another big difference in fitting the ages is that while in DR3 we worked in logarithmic space and then only converted to linear ages when plotting, in the version of PPXF used for this paper, the ages are converted into linear values in Gyr before fitting.

Indeed, as seen in Fig. B1, the scatter is large for ages and metallicities, reflecting the degeneracy between the IMF and the other stellar population parameters. This demonstrates that one needs to take it into account, even when only limiting the fit to the optical wavelength range. Overall the results from DR3 favour older ages and larger metallicity values. We remind the readers that age and metallicity are degenerate (Worthey 1994), and both quantities also

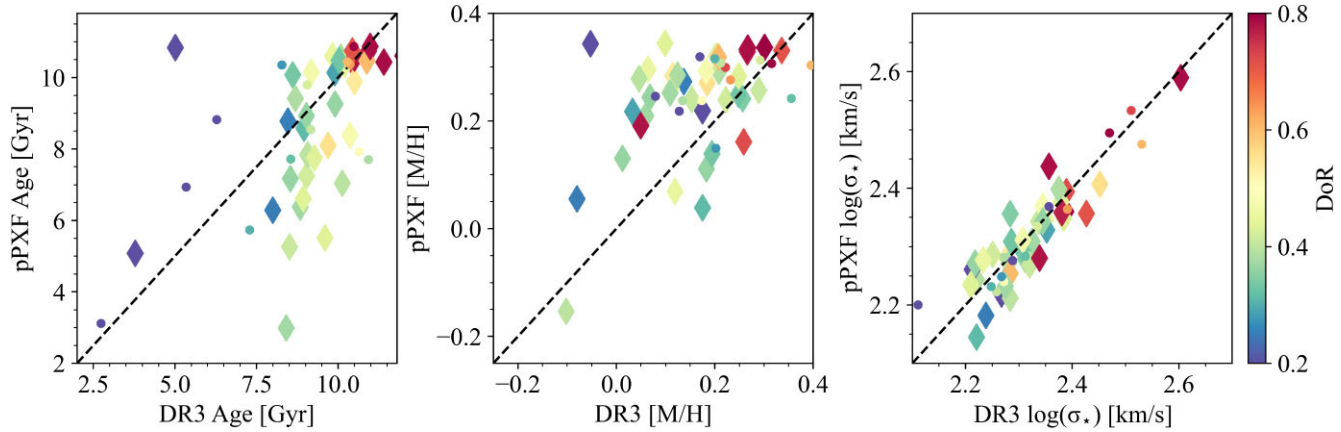

Figure B1. Comparison between the DR3 results and the ones obtained in this paper with PPXF, colour-coded by the DoR. As in previous figures, galaxies in the *Golden Sample* are shown as diamonds, although we note that these results are obtained from full-spectrum fitting, which should overcome the problem of having contamination within one or more index bandpass.

correlate with IMF (La Barbera et al. 2013; Spiniello et al. 2014; Sarzi et al. 2018; Barbosa et al. 2021b). A very good agreement is found instead for the stellar velocity dispersion values, at all DoR.

Nevertheless, as already highlighted in previous INSPIRE papers, the SFH inferred from spectral fitting depends much more on the parameters and assumptions for non-relics than for relics. This is true also in this case: we find a much better agreement for objects with DoR $\geq$ 0.6, while the scatter increases both for age and for metallicity below this value.

APPENDIX C: SPECTRAL INDICES DEFINITION

In Table C1, we provide the index definition, along with the blue and red continuum bandpasses for all the indices used in this paper. We also give the reference to the paper where each index was defined and used for the first time.

Table C1. Indices bandpasses, units in which they are measured, and papers from which they have been taken.

Line-index	Blue bandpass (Å)	Index bandpass (Å)	Red bandpass (Å)	Units	Reference
H β	[4815.000−4845.000]	[4851.320−4871.320]	[4880.000−4930.000]	Å	Vazdekis et al. (2010)
H δA	[4041.600−4079.750]	[4083.500−4122.250]	[4128.500−4161.000]	Å	Vazdekis et al. (2010)
Mg2	[4895.125−4957.625]	[5154.125−5196.625]	[5301.125−5366.125]	mag	Trager et al. (1998)
Mgb5177	[5142.625−5161.375]	[5160.125−5192.625]	[5191.375−5206.375]	Å	Trager et al. (1998)
Fe5015	[4946.500−4977.750]	[4977.750−5054.000]	[5054.000−5065.250]	Å	Trager et al. (1998)
Fe5270	[5233.150−5248.150]	[5245.650−5285.650]	[5285.650−5318.150]	Å	Trager et al. (1998)
Fe5335	[5304.625−5315.875]	[5312.125−5352.125]	[5353.375−5363.375]	Å	Trager et al. (1998)
Fe5709	[5672.875−5696.625]	[5696.625−5720.375]	[5722.875−5736.625]	Å	Trager et al. (1998)
NaD	[5860.625−5875.625]	[5876.875−5909.375]	[5922.125−5948.125]	Å	Trager et al. (1998)
TiO1	[5723.000−5750.000]	[5945.000−5994.125]	[6038.625−6103.625]	mag	Spiniello et al. (2014)
TiO2	[6066.600−6141.600]	[6189.625−6265.000]	[6422.000−6455.000]	mag	Spiniello et al. (2014)
TiO3	[7017.000−7064.000]	[7123.750−7162.500]	[7234.000−7269.000]	mag	Spiniello et al. (2014)

This paper has been typeset from a TEX/LATEX file prepared by the author.